Analytical formalism for determining quantum-wire and quantum-dot band structure in the multiband envelope-function approximation

Peter C. Sercel and Kerry J. Vahala

Department of Applied Physics, California Institute of Technology, The Thomas J. Watson, Sr. Laboratories of Applied Physics (Mail Stop 128-95), Pasadena, California 91125

We describe a new formalism for determining energy eigenstates of spherical quantum dots and cylindrical quantum wires in the multiple-band envelope-function approximation. The technique is based upon a reformulation of the $\mathbf{K \cdot P}$ theory in a basis of eigenstates of total angular momentum. Stationary states are formed by mixing bulk energy eigenvectors and imposing matching conditions across the heterostructure interface, yielding dispersion relations for eigenenergies in quantum wires and quantum dots. The bound states are studied for the conduction band and the coupled light and heavy holes as a function of radius for the $GaAs/Al_xGa_{1-x}As$ quantum dot. Conduction-band–valence-band coupling is shown to be critical in a "type-II" $InAs/GaSb$ quantum dot, which is studied here for the first time. Quantum-wire valence-subband dispersion and effective masses are determined for $GaAs/Al_xGa_{1-x}As$ wires of several radii. The masses are found to be independent of wire radius in an infinite-well model, but strongly dependent on wire radius for a finite well, in which the effective mass of the highest-energy valence subband is as low as $0.16m_0$. Implications of the band-coupling effects on optical matrix elements in quantum wires and dots are discussed.

I. INTRODUCTION

The rapid progress of experimental efforts to fabricate quantum wires and quantum dots (the two- and three-dimensional analogues of the conventional quantum well in zinc-blende-structure semiconductors) is a strong impetus to develop theoretical techniques for their study. In this paper we present a complete account of a new analytical method for this problem, first presented by the authors in Refs. 1 and 2. We show how to determine simple expressions for eigenstates and eigenenergies of the spherical quantum dot and the cylindrical quantum wire, rigorously incorporating band-coupling effects, through simple dispersion relations accessible to experimentalists, in contrast to complex numerical procedures previously required.

We begin in Sec. II with a review of the conventional approaches to the calculation of states in heterostructures, intending to show the shortcomings of existing techniques for studying quantum wires and dots so as to motivate the rest of the discussion. We find in Sec. III that the analysis of spherical quantum dots and cylindrical quantum wires in the multiband envelope-function approximation is simplified due to the high symmetry of these structures and the separable nature of their heterostructure potentials. This simplification is made possible by the observation, originally made in the context of the theory of acceptors, that total angular momentum, defined in Sec. IV, commutes with the Hamiltonian in the spherical-band-structure approximation.[3–5] We therefore proceed, in Secs. IV and VI, to develop the $\mathbf{K \cdot P}$ band-structure Hamiltonian in representations appropriate to the quantum dot and quantum wire, respectively, based on the eigenstates of this operator. Using the bulk crystal eigenstates that arise in these new representations, we construct eigenstates of the spherical quantum dot and cylindrical quantum wire in a piecewise continuous fashion across the heterostructure interface in Secs. V and VII. This leads naturally to exact solutions for the bound states. Representative calculations are performed on the coupled conduction and valence bands in quantum dots and wires to illustrate application of the formalism.

II. CONVENTIONAL TECHNIQUES FOR STUDYING QUANTUM CONFINEMENT EFFECTS IN SEMICONDUCTORS

Prior to the introduction of our technique, theoretical analyses of conduction- and valence-band states in quantum wires and dots employed either the simple one-band effective-mass analysis used initially in this field, or computational approaches based on the standard multiband envelope-function theory. The former approach, while of great value in the study of conduction-band states, breaks down fundamentally in the study of the valence bands as well as the conduction band in narrow-band-gap semiconductors. Studies which use this technique to calculate optical matrix elements and gain[6,7] and exciton states[8–10] entirely neglect band coupling, which has a profound effect on the valence-subband structure in quantum wells[11] and as shown in this work, quantum dots and quantum wires.

The latter approach, standard multiband envelope-function theory, has been applied to the study of confinement in quantum wires in an effort to correct this flaw. However, the calculations that have been performed, while including band-coupling effects, have certain other drawbacks, the foremost of which is mathematical complexity. The problem consists

mathematically of a set of coupled, simultaneous, second-order partial differential equations, one for each band included in the analysis, to be solved for envelope functions in conjunction with appropriate boundary conditions. Even the simpler problem of the valence-subband dispersion in a quantum well has an analytical solution only in the approximation of an infinite-potential barrier.[11] A more realistic model of the quantum well, with finite-band discontinuities, requires numerical solution.

The quantum-wire and quantum-dot problems are more complicated than that of the quantum well (which is essentially a one-dimensional potential problem), because these structures are multidimensional. This is depicted in Fig. 1, which shows a geometrical model of the quantum wire and quantum dot employed in much of the work that has been done in this field.[12-14] In analogy with the conventional quantum well, there is a well region of low-band-gap material with square or rectangular cross sections embedded in a higher-band-gap barrier region, so that the structures have planar interfaces. However, the finite heterostructure potential is nonseparable in this case, a serious complication even in the simple one-band problem. As such, workers studying quantum wires frequently resort to the use of infinite-well barriers to simplify the problem mathematically[13]—an approach which can cause certain interesting physical effects to be overlooked,[15,16] while still leaving a complex problem. Other workers have retained finite barriers in their model, employing approximation methods[12] or more computationally intensive approaches.[14,17] While these studies are valuable, the relationship between the physics of the structures and fundamental parameters is, therefore, somewhat obscured, a quality which reduces usefulness to experimentalists and device engineers.

An alternate approach is to use a model characterized by separable finite potentials, as in the cylindrical quantum wire and the spherical quantum dot depicted in Fig. 2. These high-symmetry geometries greatly simplify the mathematics of the problem to be solved, so that an

Spherical Quantum Dot:

Cylindrical Quantum Wire:

FIG. 2. A cylindrical quantum wire and a spherical quantum dot. The drawings to the left represent the structures, those to the right represent the confining potential as a function of the radial coordinate in each case. The well depth, V_0 in the figure, represents a discontinuity of the band edges across the heterostructure interface.

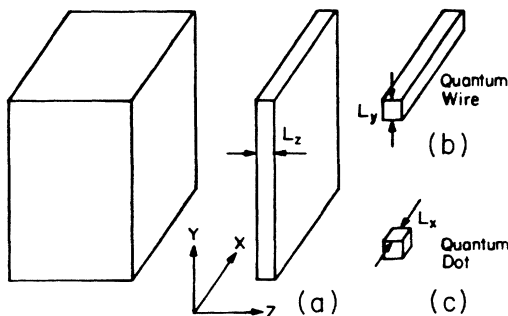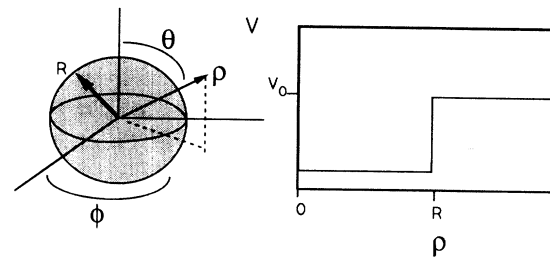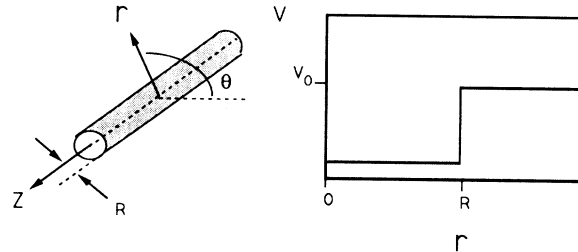Quantum Wells, Quantum Wires, and Quantum Dots

FIG. 1. Quantum wells, quantum wires, and quantum dots. The cube on the left represents bulk semiconductor. The drawings labeled (a), (b), and (c) represent quantum-well, quantum-wire, and quantum-dot structures, respectively, with planar boundaries.

analytical solution might be expected, while retaining the fundamental features of the problem: namely, two- and three-dimensional quantum confinement, with finite-well depths. Furthermore, the cylindrical and spherical configurations are reasonable approximations to actual quantum-wire and quantum-dot nanostructure geometries, which lack the planar interfaces characteristic of the conventional quantum well.[18-21] These geometries have, therefore, been used frequently in one-band calculations.[10,15,16] Additionally, valence-band states in quantum wire and dots with these geometries have been studied in the infinite-well approximation by an elegant coupled-band technique which is specific to the holes.[22,23] In Sec. III we will develop a general formalism for incorporating band-coupling effects among the conduction and valence bands in quantum dots and wires, building upon simplifying techniques originally developed for another centrosymmetric problem, that of charged impurities.

III. THE ENVELOPE-FUNCTION METHOD IN CENTROSYMMETRIC PROBLEMS

The starting point of the envelope-function techniques, which have been used so effectively in the study of quantum wells and Coulombic impurities, is the $\mathbf{K} \cdot \mathbf{P}$ theory of band structure.[24-27] The technique begins with the Bloch form for the energy eigenstates of a periodic potential

$$\psi_{\mathbf{K}}^j = u_{\mathbf{K}}^j(\mathbf{r})\exp(i\mathbf{K}\cdot\mathbf{r}) , \tag{1}$$

where $u^j_K(\mathbf{r})$ has the periodicity of the crystal lattice and j is a band index. At the band edges these functions are characterized by symmetry arguments as eigenstates $|J, J_z\rangle$ of an angular momentum $\mathbf{J}$, which we shall refer to as Bloch angular momentum. These are given for the conduction and valence bands in the Appendix. Using these functions as a basis, one can develop a representation $H(\mathbf{K})$ for the Hamiltonian governing the conduction and valence bands (such as that given in the Appendix, Table V).

To find heterostructure or impurity states, a potential $V(\mathbf{r})$ modeling the problem is added to the Hamiltonian. A solution is assumed of the form

$$\psi = \sum_{J, J_z} |J, J_z\rangle F_{J, J_z}(\mathbf{r}) , \qquad (2)$$

where F is an envelope function which replaces the plane waves of the perfect periodic crystal, and the sum may include conduction and valence bands. $\mathbf{K}$ is replaced by $-i\hbar\nabla$ in the Hamiltonian $H(\mathbf{K})$, creating a differential operator which acts on the envelope functions. We are left with an effective envelope Schrödinger equation,[11,26,27]

$$\sum_j [H_{ij}(-i\hbar\nabla) + V(\mathbf{r})] F_j(\mathbf{r}) = E F_i(\mathbf{r}) , \qquad (3)$$

where we use the simplified notation (i, j) in place of angular momentum quantum numbers, to represent band indices. In conjunction with appropriate boundary conditions this coupled set of equations is solved for the envelope functions.

Extensive work done on the Coulomb impurity problem for degenerate valence bands has established several important results applicable to our problem. The first is that, in most materials of interest (with the notable exception of silicon), it is acceptable, at least as a first-order approximation, to replace anisotropic terms in the $\mathbf{K} \cdot \mathbf{P}$ Hamiltonian by a suitable spherical average, neglecting "warping" terms of cubic symmetry.[4,5] In such a spherical approximation, the sum of the angular momenta, $\mathbf{J}$ of the band-edge Bloch functions and $\mathbf{L}$ of the envelope functions, is a constant of the motion.[3-5] We call this conserved operator the "total angular momentum," $\mathbf{F} = \mathbf{J} + \mathbf{L}$. Based on this result, Baldereschi and Lipari[4,5] utilized an analogy between $\mathbf{L}$ and $\mathbf{J}$ and the L-S coupling scheme used in atomic physics to greatly simplify the acceptor-state problem. The role of the atomic-orbital wave function is assumed by the envelopes. Instead of the electron spin $\frac{1}{2}$ the "spin" in the acceptor-state problem assumes the value $J = \frac{3}{2}$, which characterizes the underlying band-edge Bloch states of the light and heavy holes (the Γ_8 states). The acceptor wave functions are then simplified by application of the theory of angular momentum, and computed variationally using Eq. (3) without the warping terms. The warping can be added as a small perturbation if desired.[5]

Two important features emerge in applying this formalism to a centrosymmetric heterostructure problem. The first is that, whereas the wave functions and energy levels of the acceptor-state problem must be computed

variationally, and then corrected approximately for such effects as the "central-cell" overlap of the wave function, we can expect exact solutions for flat-band quantum-dot or quantum-wire heterostructures. Second, the formalism must be generalized if it is to be applicable to problems other than the coupled light- and heavy-hole bands. In narrow band-gap semiconductors, for example, coupling between the conduction and valence bands causes appreciable nonparabolicity in the band structure.[24] To incorporate such effects, it will be necessary to treat the $\mathbf{K} \cdot \mathbf{P}$ coupling term between the conduction and valence bands explicitly in developing the envelope Hamiltonian. However, the conduction band is characterized by $J = \frac{1}{2}$, different from that of the $J = \frac{3}{2}$ states to which the acceptor-state problem is restricted, so that in a direct application of the formalism developed for acceptors, the envelope-state spin evidently has internal variables. In light of this, we have developed a more general analogy. We imagine a two-particle system comprised of an "envelope" particle and a "Bloch" particle, with respective angular momenta $\mathbf{L}$ and $\mathbf{J}$, and total angular momentum $\mathbf{F} = \mathbf{J} + \mathbf{L}$, as before. Thus the model reduces to the formalism developed for the acceptor problem in the case of the Γ_8 states. However, in contrast to the orbit-spin analogy of Baldereschi and Lipari, we will see that this model incorporates the direct $\mathbf{K} \cdot \mathbf{P}$ coupling term between the conduction and valence bands in a natural way, through the kinetic energy of the two-particle couple. Furthermore, the model emerges naturally in the context of the envelope-function approximation.

A subtle feature of the theory leading to Eq. (3) illustrates the last point. In replacing $\mathbf{K}$ by the operator $-i\hbar\nabla$ which acts only on the envelope functions F_j, we have implicitly treated the envelopes F_j and the underlying Bloch functions $|J, J_z\rangle$ as functions of spatial coordinates corresponding to different states spaces. Examination of how wave functions developed in the envelope theory are used to calculate observables confirms this interpretation—the envelope and Bloch parts of matrix elements factor into separate integrals. A familiar example is the K-selection rule for band-to-band optical transitions in bulk semiconductors or quantum wells.[28] This factoring is a result of the separate nature of the envelope and Bloch function state spaces. The Bloch functions u^j_K are defined in a coordinate space "interior" to the unit cell, while the envelope functions F_i are essentially defined over the lattice points, in a coarse-grain approximation valid for describing functions which are slowly varying on the scale of the unit cell of the crystal.

The total wave function, which describes a carrier, exists in a composite state space, which is a direct sum of the envelope space and the Bloch space. Operators pertaining to the envelope space commute with those belonging to the Bloch space. The two spaces are coupled through the kinetic energy of the carrier they describe. This is given by $T = |\mathbf{P}|^2 / 2m_0$, where m_0 is the free-electron mass and $\mathbf{P}$ is its momentum, equal to the sum of the momenta of the Bloch and envelope "particles," $\mathbf{P} = \mathbf{P}_B + \mathbf{P}_e$. We note that this seems equivalent to a classical "center-of-mass" momentum of the two-particle

couple. However, in contrast to a system of two real particles, there is no relative coordinate in our model, since the envelope and Bloch particles pertain to the same physical carrier. Thus, the kinetic energy takes the form

$$T = |\mathbf{P}|^2/2m_0 = \frac{|\mathbf{P}_B|^2 + |\mathbf{P}_e|^2 + 2\mathbf{P}_B \cdot \mathbf{P}_e}{2m_0} , \quad (4)$$

which is invariant with respect to the total angular momentum $\mathbf{F}$. If we represent this in a basis of the Bloch form, Eq. (1), the matrix element of $\mathbf{P}_B \cdot \mathbf{P}_e$ becomes the $\mathbf{K} \cdot \mathbf{P}$ of conventional band-structure theory, $|\mathbf{P}_B|^2$ is incorporated in the band edges $E(0)$, and $|\mathbf{P}_e|^2$ enters the free-electron kinetic energy term. Thus, the two-particle model leads to the full $\mathbf{K} \cdot \mathbf{P}$ Hamiltonian governing valence as well as conduction bands in an intuitive way. As in the (less general) acceptor formalism, the total angular momentum is a constant of the motion in the absence of anisotropic coupling to remote bands.

We can, therefore, take full advantage of theory of angular momentum in the centrosymmetric heterostructure problems at hand. For example, a basis of common eigenstates of the Hamiltonian H, the operator $\mathbf{F}^2$, and the projection of total angular momentum along the quantization axis F_z will greatly simplify problems with spherical symmetry such as the spherical quantum dot. The common eigenstates of H, F_z, and P_z, the component of envelope linear momentum along the z axis will similarly profit us in the cylindrical–quantum-wire problem.

IV. BAND STRUCTURE IN A SPHERICAL REPRESENTATION

We found in Sec. III that the set of operators $(H, \mathbf{F}^2, F_z)$ form a complete set of commuting observables

for the band-structure Hamiltonian in the absence of anisotropic remote band coupling. This makes sense intuitively; we expect the Hamiltonian of our two-particle system to be a scalar with respect to the total angular momentum in the absence of anisotropic interactions.

The conceptual model that we have adopted amounts to replacing a finite symmetry group, the space group of the crystal, with the full rotation group. We reiterate that this simplification requires a spherical band-structure approximation. In the Kane model,[24,25] coupling of the valence and conduction bands is isotropic and the effects of remote bands not explicitly included in the analysis are ignored, so that this requirement is automatically satisfied. Many problems, however, necessitate the use of the generalized Hamiltonian given in the Appendix, which additionally incorporates Luttinger-type coupling terms among the valence bands.[27] These terms represent indirect coupling via remote bands, and generally impart cubic symmetry to the band structure. However, many materials are modeled well by setting the Luttinger parameters γ_2 and γ_3 equal, in which case this coupling becomes isotropic.[4] For greater accuracy, band warping terms in $\gamma_2 - \gamma_3$ can be introduced later as a perturbation.[5]

In a spherical approximation, the Hamiltonian will be block diagonal in a basis of eigenstates of $\mathbf{F}^2$ and F_z, assuming the form

$$\underline{H} = \sum_{F, F_z} \underline{H}_{F, F_z} . \quad (5)$$

Using the familiar rules of addition of angular momentum we form such a basis as follows:

$$|K; F; F_z; J, L\rangle = \sum_{J_z = -J}^{J} \sum_{L_z = -L}^{L} \langle J, J_z; L, L_z | F, F_z \rangle |J, J_z\rangle |K; L, L_z\rangle . \quad (6)$$

The first term in the sum is the Clebsch-Gordan coefficient for adding states of angular momenta $\mathbf{J}$ and $\mathbf{L}$. The states $|J, J_z\rangle$ as before are the band-edge functions of the Bloch state space, explicitly given in the Appendix, and $|K; L, L_z\rangle$ are envelope functions with angular momentum quantum numbers L and L_z.

We anticipate that the appropriate envelope basis for a flat-band region consists of free spherical waves. The envelope kets $|K; L, L_z\rangle$, therefore, have the coordinate representations

$$\langle \rho, \theta, \phi | K, L, L_z \rangle = \sqrt{2/\pi} i^L h_L(K\rho) Y_L^{L_z}(\theta, \phi) , \quad (7)$$

where h_L is a spherical Hankel function, $Y_L^{L_z}$ is a spherical harmonic, and K is the radial wave number. These envelope functions form a complete set in the envelope state space, obeying the orthonormality relation

$$\langle K, L, L_z | K', L', L_z' \rangle = \frac{\delta(K - K')}{K^2} \delta_{L, L'} \delta_{L_z, L_z'} , \quad (8)$$

and the envelope-space closure relation

$$\mathbf{1}_e = \sum_{L=0}^{\infty} \sum_{L_z = -L}^{L} \int_0^\infty K^2 dK |K, L, L_z\rangle \langle K, L, L_z| . \quad (9)$$

To obtain the explicit form of the band-structure Hamiltonian, Eq. (5), in the total angular momentum representation $|K; F, F_z; J, L\rangle$, we apply a unitary basis transformation to the Hamiltonian matrix given in the conventional Bloch plane-wave basis, $|\mathbf{K}; J, J_z\rangle = |\mathbf{K}\rangle |J, J_z\rangle$. We begin by establishing the relationship between the plane-wave envelope states $|\mathbf{K}\rangle$ and the spherical-wave envelope states just introduced:

$$|\mathbf{K}\rangle = \sum_{L, L_z} [Y_L^{L_z}(\Omega_\mathbf{K})]^* |K, L, L_z\rangle . \quad (10)$$

In this equation $\Omega_K = (\theta_K, \phi_K)$ are the polar coordinates of the vector K. Projection of this relationship onto the bra $\langle K', L', L_z' |$, using Eq. (8), results in the following unitary transformation matrix relating the two envelope bases:

$$\langle K', L', L_z' | K \rangle = [Y_{L'}^{L_z'}(\theta_K, \phi_K)]^* \frac{\delta(K - K')}{K^2} . \quad (11)$$

Next, we write the closure relation for the product Bloch plane-wave basis:

$$1 = 1_B \otimes 1_e = \left[\sum_{J, J_z} |J, J_z\rangle \langle J, J_z| \right]$$

$$\otimes \left[\int dk \, K^2 \int d\Omega_K |K\rangle\langle K| \right] , \quad (12)$$

where the subscripts e and B denote envelope space and Bloch space, respectively. We insert this closure relation into the expression for the components of a state ψ written in the total angular momentum basis:

$$\langle K; F, F_z; J, L | \psi \rangle = \langle K; F, F_z; J, L | \left[\sum_{J', J_z'} |J', J_z'\rangle \langle J', J_z'| \right] \left[\int dK' \, (K')^2 \int d\Omega_{K'} |K'\rangle\langle K'| \right] |\psi\rangle . \quad (13)$$

Using Eqs. (6) and (11), this results in

$$\langle K, F, F_z; J, L | \psi \rangle = \sum_{J_z = -J}^{J} \sum_{L_z = -L}^{L} \langle J, J_z; L, (L_z = F_z - J_z) | F, F_z \rangle \int d\Omega_K [Y_L^{L_z}(\Omega_K)]^* \langle K; J, J_z | \psi \rangle , \quad (14)$$

which is the required unitary transformation. We use this to derive an expression giving the matrix elements of the $K \cdot P$ Hamiltonian in the basis of eigenstates of F:

$$\langle K, F, F_z; J, L | H | K, F', F_z'; J', L' \rangle = \sum_{J_z = -J}^{J} \sum_{J_z' = -J'}^{J'} \langle J, J_z; L, (L_z = F_z - J_z) | F, F_z \rangle \langle J', J_z'; L', (L_z = F_z' - J_z') | F', F_z' \rangle$$

$$\times \int d\Omega_K [Y_L^{(F_z - J_z)}(\Omega_K)]^* [Y_{L'}^{(F_z' - J_z')}(\Omega_K)]$$

$$\times \langle K; J, J_z | H | K; J', J_z' \rangle . \quad (15)$$

The matrix elements $\langle K; J, J_z | H | K; J', J_z' \rangle$ belong to the conventional $K \cdot P$ Hamiltonian written in the basis of zone-center Bloch functions. We used the fact that this matrix does not mix waves of different K to eliminate one integration in (15). For reference, we give the full Hamiltonian in the conventional basis in the Appendix.

Using the transformation equation (15), we have derived the explicit form of the band-structure Hamiltonian Eq. (5) in our spherical-wave representation. Since states of different total angular momentum do not couple, it is most useful to present each angular momentum subblock $\underline{H}_{F, F_z}$ separately. We begin with the two degenerate subspaces corresponding to $F = \frac{1}{2}, F_z = \pm\frac{1}{2}$. It is simple to show that for the conduction- and valence-band system, these blocks are each six dimensional, each subspace being spanned by the two possible kets from each of the band edges that can be constructed with $F_z = \pm\frac{1}{2}$. For reference, the explicit form of these basis vectors are shown in Table I. We use the notation $|J, L\rangle$ for our basis with the quantum numbers $F = \frac{1}{2}$ and $F_z = \pm\frac{1}{2}$ in $|F, F_z; J, L\rangle$ understood and therefore omitted.

In Eq. (16), $P = -i\langle s | P_z^B | z \rangle$ is equivalent to the Kane momentum matrix element.[24,25] Atomic units are used throughout this paper. $E_c, E_v, E_v - \Delta$ denote the

conduction-band edge, heavy-hole and light-hole band edges, and split-off band edges, respectively. The γ parameters in this full matrix are the so-called "modified" Luttinger parameters which are related to the "true" Luttinger coupling parameters by the relations[29]

$$\gamma_1 = \gamma_1^{\text{true}} - \frac{2P^2}{3(E_c - E_v)} ,$$

$$\gamma_2 = \gamma_2^{\text{true}} - \frac{P^2}{3(E_c - E_v)} . \quad (17)$$

In Luttinger's original work[27] the conduction band was treated as remote, hence the above correction is necessary when the conduction-band coupling is treated explicitly.

From selection rules for parity, Hamiltonian block $\underline{H}_{\frac{1}{2}, \pm\frac{1}{2}}$ can be further decomposed to

$$\underline{H}_{\frac{1}{2}, \pm\frac{1}{2}} = \begin{bmatrix} \underline{H}^{l=0} & \underline{0} \\ \underline{0} & \underline{H}^{l=1} \end{bmatrix} , \quad (18)$$

where the blocks $\underline{H}^{l=\{0,1\}}$ take the form

$$
H_{\frac{1}{2},\pm\frac{1}{2}}=
\begin{array}{c|cccccc}
 & |\tfrac{1}{2},1\rangle & |\tfrac{1}{2},0\rangle & |\tfrac{3}{2},1\rangle & |\tfrac{3}{2},2\rangle & |\tfrac{1}{2},0\rangle & |\tfrac{1}{2},1\rangle \\
\hline
|\tfrac{1}{2},1\rangle & E_c+\tfrac{1}{2}K^2 & 0 & 0 & -i\sqrt{2/3}PK & -i\sqrt{1/3}PK & 0 \\
|\tfrac{1}{2},0\rangle & 0 & E_c+\tfrac{1}{2}K^2 & -i\sqrt{2/3}PK & 0 & 0 & -i\sqrt{1/3}PK \\
|\tfrac{3}{2},1\rangle & 0 & i\sqrt{2/3}PK & E_v-(\gamma_1+2\gamma_2)\dfrac{K^2}{2} & 0 & 0 & -2\sqrt{2}\gamma_2\dfrac{K^2}{2} \\
|\tfrac{3}{2},2\rangle & i\sqrt{2/3}PK & 0 & 0 & E_v-(\gamma_1+2\gamma_2)\dfrac{K^2}{2} & -2\sqrt{2}\gamma_2\dfrac{K^2}{2} & 0 \\
|\tfrac{1}{2},0\rangle & i\sqrt{1/3}PK & 0 & 0 & -2\sqrt{2}\gamma_2\dfrac{K^2}{2} & E_v-\Delta-\gamma_1\dfrac{K^2}{2} & 0 \\
|\tfrac{1}{2},1\rangle & 0 & i\sqrt{1/3}PK & -2\sqrt{2}\gamma_2\dfrac{K^2}{2} & 0 & 0 & E_v-\Delta-\gamma_1\dfrac{K^2}{2}
\end{array}
. \quad (16)
$$

TABLE I. Explicit representations for basis states of total angular momentum corresponding to quantum numbers $F=\frac{1}{2}$ and $F_z=\frac{1}{2}$. The heavy holes are not contained in the $F=\frac{1}{2}$ space, as discussed in the text. The $f_l(K\rho)$ are spherical Bessel functions or spherical Hankel functions.

Band	$|J,L\rangle$	Basis vectors for $F=\frac{1}{2}, F_z=+\frac{1}{2}$ Explicit representation	Radial envelope
Conduction band	$|\frac{1}{2},0\rangle$	$|\frac{1}{2},\frac{1}{2}\rangle\otimes|K,0,0\rangle$	$f_0(K\rho)$
(Γ_6)	$|\frac{1}{2},1\rangle$	$\sqrt{1/3}|\frac{1}{2},\frac{1}{2}\rangle\otimes|K,1,0\rangle-\sqrt{2/3}|\frac{1}{2},-\frac{1}{2}\rangle\otimes|K,1,1\rangle$	$f_1(K\rho)$
Light holes	$|\frac{3}{2},1\rangle$	$\sqrt{1/2}|\frac{3}{2},\frac{3}{2}\rangle\otimes|K,1,-1\rangle-\sqrt{1/3}|\frac{3}{2},\frac{1}{2}\rangle\otimes|K,1,0\rangle+\sqrt{1/6}|\frac{3}{2},-\frac{1}{2}\rangle\otimes|K,1,1\rangle$	$f_1(K\rho)$
(Γ_8)	$|\frac{3}{2},2\rangle$	$\sqrt{1/10}|\frac{3}{2},\frac{3}{2}\rangle\otimes|K,2,-1\rangle-\sqrt{1/5}|\frac{3}{2},\frac{1}{2}\rangle\otimes|K,2,0\rangle+\sqrt{3/10}|\frac{3}{2},-\frac{1}{2}\rangle\otimes|K,2,1\rangle-\sqrt{2/5}|\frac{3}{2},-\frac{3}{2}\rangle\otimes|K,2,2\rangle$	$f_2(K\rho)$
Split-off band	$|\frac{1}{2},0\rangle$	$|\frac{1}{2},\frac{1}{2}\rangle\otimes|K,0,0\rangle$	$f_0(K\rho)$
(Γ_7)	$|\frac{1}{2},1\rangle$	$\sqrt{1/3}|\frac{1}{2},+\frac{1}{2}\rangle\otimes|K,1,0\rangle-\sqrt{2/3}|\frac{1}{2},-\frac{1}{2}\rangle\otimes|K,1,1\rangle$	$f_1(K\rho)$

$$
\underline{H}^{I=\{0,1\}} =
\begin{array}{c}
 \\
|\tfrac{1}{2},\{0,1\}\rangle \\
|\tfrac{3}{2},\{1,2\}\rangle \\
|\tfrac{1}{2},\{0,1\}\rangle
\end{array}
\begin{array}{ccc}
|\tfrac{1}{2},\{0,1\}\rangle & |\tfrac{3}{2},\{1,2\}\rangle & |\tfrac{1}{2},\{1,0\}\rangle \\
\left[\begin{array}{ccc}
E_c + \tfrac{1}{2}K^2 & -i\sqrt{2/3}PK & -i\sqrt{1/3}PK \\
i\sqrt{2/3}PK & E_v - (\gamma_1 + 2\gamma_2)\dfrac{K^2}{2} & -2\sqrt{2}\gamma_2\dfrac{K^2}{2} \\
i\sqrt{1/3}PK & -2\sqrt{2}\gamma_2\dfrac{K^2}{2} & E_v - \Delta - \gamma_1\dfrac{K^2}{2}
\end{array}\right]
\end{array}
\tag{19}
$$

The envelope angular momentum quantum number is to be read as the first or second number in the curly brackets $\{i,j\}$. Other than this, the two blocks assume identical forms.

When we diagonalize these blocks, we obtain eigenvalues corresponding to the light holes, split-off holes, and the conduction electrons. This is most easily seen if we make certain simplifications. If we consider the case, equivalent to the Kane model,[24,25] in which all the higher band coupling terms and the free-electron energy are neglected, we recover the nonparabolic dispersion relation

$$
(E_c - E)(E_v - E)(E_v - \Delta - E) = (E_v - \tfrac{2}{3}\Delta - E)P^2 K^2 ,
\tag{20}
$$

which is the well-known result for the split-off, light hole, and conduction bands. If Δ is large, we can describe the coupled electrons and light holes with the two-band dispersion relation

$$
(E_c - E)(E_v - E) = \tfrac{2}{3}P^2 K^2 .
\tag{21}
$$

On the other hand, considering only the Γ_8 states, treating the conduction bands and the split-off bands as remote, we immediately see that the states $|\tfrac{3}{2},1\rangle$ and $|\tfrac{3}{2},2\rangle$ decouple with eigenvalues $E(K) = E_v - (\gamma_1 + 2\gamma_2)K^2/2$, as we expect for the light holes. Again, the heavy-hole states are not found in this subspace.

These observations lead us to point out that states must be labeled "light hole" or "heavy hole" solely on the basis of the eigenvalue dispersion, $E(K)$, to which the states correspond, and not on the basis of the quantum number J_z of the Bloch component of the wave function, $|J,J_z\rangle$, as some authors prefer. The eigenstates of the conventional Luttinger Hamiltonian for $\mathbf{K} = K\hat{z}$ correspond to $J_z = \pm\tfrac{1}{2}$ for the light holes and $J_z = \pm\tfrac{3}{2}$ for the heavy holes.[26,27] However, J_z is generally not a good quantum number and this correspondence does not hold for all directions of the vector $\mathbf{K}$. In fact, the light-hole states $|\tfrac{3}{2},1\rangle$ and $|\tfrac{3}{2},2\rangle$ discussed above are superpositions involving various $|J,J_z\rangle$, as shown in Table I. (It remains true, however, that a projection of either state onto the space of Bloch eigenstates with $\mathbf{K} = K\hat{z}$, recovers a superposition of Bloch states characterized by $J_z = \pm\tfrac{1}{2}$.)

The heavy holes first appear in the four degenerate spaces corresponding to $F = \tfrac{3}{2}$, and its four projections $F_z = \pm\tfrac{1}{2}$ and $F_z = \pm\tfrac{3}{2}$. These are each spanned by eight vectors. As before we find that each of these sets decouple into 2 subsets of four vectors, due to parity selection rules. The four degenerate Hamiltonian subblocks thus each assume the form

$$
\underline{H}_{\tfrac{3}{2},\,\pm\tfrac{1}{2}\text{ or }\pm\tfrac{3}{2}} =
\begin{bmatrix}
\underline{H}^1 & 0 \\
0 & \underline{H}^2
\end{bmatrix} ,
\tag{22}
$$

with the parity subblocks given respectively by

$$
\underline{H}^1 =
\begin{array}{c}
|\tfrac{1}{2},1\rangle \\
|\tfrac{3}{2},0\rangle \\
|\tfrac{3}{2},2\rangle \\
|\tfrac{1}{2},2\rangle
\end{array}
\begin{array}{cccc}
|\tfrac{1}{2},1\rangle & |\tfrac{3}{2},0\rangle & |\tfrac{3}{2},2\rangle & |\tfrac{1}{2},2\rangle \\
\left[\begin{array}{cccc}
E_c + \tfrac{1}{2}K^2 & i\sqrt{1/3}PK & -i\sqrt{1/3}PK & -i\sqrt{1/3}PK \\
-i\sqrt{1/3}PK & E_v - \gamma_1\dfrac{K^2}{2} & 2\gamma_2\dfrac{K^2}{2} & 2\gamma_2\dfrac{K^2}{2} \\
i\sqrt{1/3}PK & 2\gamma_2\dfrac{K^2}{2} & E_v - \gamma_1\dfrac{K^2}{2} & -2\gamma_2\dfrac{K^2}{2} \\
i\sqrt{1/3}PK & 2\gamma_2\dfrac{K^2}{2} & -2\gamma_2\dfrac{K^2}{2} & E_v - \Delta - \gamma_1\dfrac{K^2}{2}
\end{array}\right]
\end{array}
\tag{23}
$$

and

$$\underline{H}^2 = \begin{array}{c} \\ |\tfrac{1}{2},2\rangle \\ |\tfrac{3}{2},1\rangle \\ |\tfrac{3}{2},3\rangle \\ |\tfrac{1}{2},1\rangle \end{array} \begin{array}{cccc} |\tfrac{1}{2},2\rangle & |\tfrac{3}{2},1\rangle & |\tfrac{3}{2},3\rangle & |\tfrac{1}{2},1\rangle \\ \left| \begin{array}{cccc} E_c + \tfrac{1}{2}K^2 & i\sqrt{1/15}\,PK & -i\sqrt{3/15}\,PK & -i\sqrt{1/3}\,K \\[6pt] -i\sqrt{1/15}\,PK & E_v-(\gamma_1-\tfrac{8}{5}\gamma_2)\dfrac{K^2}{2} & \dfrac{6}{5}\gamma_2\dfrac{K^2}{2} & \dfrac{2}{\sqrt{5}}\gamma_2\dfrac{K^2}{2} \\[10pt] i\sqrt{3/5}\,PK & \dfrac{6}{5}\gamma_2\dfrac{K^2}{2} & E_v-(\gamma_1+\tfrac{8}{5}\gamma_2)\dfrac{K^2}{2} & -\dfrac{6}{\sqrt{5}}\gamma_2\dfrac{K^2}{2} \\[10pt] i\sqrt{1/3}\,PK & \dfrac{2}{\sqrt{5}}\gamma_2\dfrac{K^2}{2} & -\dfrac{6}{\sqrt{5}}\gamma_2\dfrac{K^2}{2} & E_v-\Delta-\gamma_1\dfrac{K^2}{2} \end{array} \right| \end{array}, \qquad (24)$$

where the quantum numbers F, F_z have again been omitted in the vectors. Diagonalization of these matrices yields the conduction, light-hole (LH), heavy-hole (HH), and split-off band eigenvectors for these spaces. It is interesting to examine the form of these matrices after application of a unitary transformation which diagonalizes the inner 2×2 system, which represents the projection of the Hamiltonian onto the Γ_8 band edge. For example, transformation of the inner block in (23) using the basis vector definitions: $|\text{LH}\rangle = (|\tfrac{3}{2},0\rangle - |\tfrac{3}{2},2\rangle)/\sqrt{2}$ and $|\text{HH}\rangle = (|\tfrac{3}{2},0\rangle + |\tfrac{3}{2},2\rangle)/\sqrt{2}$, yields

$$\underline{H}^{l'} = \begin{array}{c} \\ |\tfrac{1}{2},1\rangle \\ |\text{LH}\rangle \\ |\text{HH}\rangle \\ |\tfrac{1}{2},2\rangle \end{array} \begin{array}{cccc} |\tfrac{1}{2},1\rangle & |\text{LH}\rangle & |\text{HH}\rangle & |\tfrac{1}{2},2\rangle \\ \left| \begin{array}{cccc} E_c+1/2K^2 & i\sqrt{2/3}\,PK & 0 & -i\sqrt{1/3}\,PK \\[6pt] -i\sqrt{2/3}\,PK & E_v-(\gamma_1+2\gamma_2)\dfrac{K^2}{2} & 0 & 2\sqrt{2}\gamma_2\dfrac{K^2}{2} \\[10pt] 0 & 0 & E_v-(\gamma_1-2\gamma_2)\dfrac{K^2}{2} & 0 \\[10pt] i\sqrt{1/3}\,PK & 2\sqrt{2}\gamma_2\dfrac{K^2}{2} & 0 & E_v-\Delta-\gamma_1\dfrac{K^2}{2} \end{array} \right| \end{array}. \qquad (25)$$

It is clear that the vector $|\text{HH}\rangle$, which is decoupled from all other states, belongs to the heavy-hole band. The conduction, light-hole and split-off bands are coupled. Interestingly, this is the same matrix that one obtains with the conventional theory, when **K** is directed along the z axis. In the present case, however, the coupling parameter is the isotropic radial wave number K.

As before, it is useful to explore certain simplifying limiting cases. If the spin-orbit parameter Δ and the energy gap E_c-E_v are large compared to the kinetic energies of the light holes, we can treat the split-off and conduction bands as remote. In this case, the γ's are true Luttinger parameters and we retain only the Γ_8 block of the matrix in (25). Then the vector $|\text{LH}\rangle$ is rigorously identified as the light-hole eigenstates, with the familiar eigenvalues $E(K)=E_v-(\gamma_1+2\gamma_2)K^2/2$. On the other hand, in the limit where the terms in K^2 can be neglected, we again retrieve the Kane dispersion relations, Eqs. (20) and (21), plus one more for the heavy holes: $E_{\text{HH}}=E_v$. The heavy-hole band is entirely flat in this approximation.

Continuing in this fashion, the Hamiltonian could be developed for spaces of higher angular momentum. Having demonstrated that our technique for computing band structure in a spherical representation gives the correct bulk crystal dispersion relations within a spherical band-structure approximation, we now apply the technique to the calculation of states in the spherical quantum dot in Sec. V.

V. ELECTRONIC STRUCTURE OF THE SPHERICAL QUANTUM DOT

Since the spherical quantum-dot heterostructure is an isotropic potential, F and F_z remain good quantum numbers. Thus the quantum dot may be very simply modeled by considering the band-structure parameters in our Hamiltonian subblocks as functions of the radial coordinate ρ. The states are governed by the Hamiltonian matrices $\underline{H}_{F,F_z}$ in each separate total angular momentum subspace. Consequently, the approach is algebraic, and, with only minor exceptions, is identical to that used in standard heterostructure envelope calculations.[30]

As a first example, we compute the two lowest energy conduction-band states in a GaAs quantum dot of radius R embedded in $Al_xGa_{1-x}As$. We will compare our results against those of the one-band model, which is accurate in this case, as a check of the formalism. In this simple problem, coupling to remote bands is negligible. We neglect the free-electron energy term and coupling to the split-off bands. The lowest states turn out to be contained in the $F=\tfrac{1}{2}$ subspace. The Hamiltonian in this case becomes a simple two-band, 2×2 matrix with band-structure constants E_c^I, E_v^I within the structure and E_c^0, E_v^0 exterior to the structure. Eigenvectors of the 2×2 Hamiltonian are computed interior and exterior to the quantum dot. We require that the wave function be regular at the origin. Boundary conditions are then applied at the interface of the dot to arrive at a relation between spheri-

cal wave numbers inside and outside. This condition is combined with the known energy dispersion relations to determine the eigenvalues of the quantum dot. The energy dispersion relations follow from Eq. (21) and are given by the expressions

$$(E_c^I - E)(E_v^I - E) = \tfrac{2}{3}P^2 k^2 ,$$

$$(E_c^0 - E)(E_v^0 - E) = -\tfrac{2}{3}P^2 \lambda^2 ,$$

(26)

where the exterior spherical wave number is taken as $i\lambda$ in anticipation of solving for bound energy eigenstates. Eigenvectors resulting from the diagonalization process have the form

$$|\psi_E\rangle = A \left[|\tfrac{1}{2}, l\rangle + \left[\frac{E - E_c}{E - E_v} \right]^{1/2} |\tfrac{3}{2}, l+1\rangle \right] , \quad (27)$$

where $l = 0, 1$ depending on the parity of the conduction-band envelope and where A is a constant to be determined by matching boundary conditions and applying normalization. The angular dependence and Bloch space elements of Eq. (27) are the same inside and outside the dot, so this vector is projected onto only the envelope-space radial coordinate representation. This results in the following two-dimensional column vector:

$$\psi_E(\rho) = A \begin{bmatrix} h_l(k\rho) \\ \left[\dfrac{E - E_c}{E - E_v}\right]^{1/2} h_{l+1}(k\rho) \end{bmatrix} . \quad (28)$$

The form of Eq. (26) is such that $\pm k$ ($\pm\lambda$) are degenerate roots. Using these roots and the basic form given by Eq. (28), state functions within each region are constructed. The requirement of regularity at the origin leads to combinations of Hankel functions within the quantum dot that are equivalent to spherical Bessel functions of the first kind. Outside the quantum dot, only the Hankel function of imaginary argument which decays for large ρ is retained. Applying continuity of the resulting envelope states at the boundary of the quantum dot leads to the following condition:

$$\frac{j_l(kR)h_{l+1}(i\lambda R)}{j_{l+1}(kR)h_l(i\lambda R)} = \left[\frac{(E - E_c^I)(E - E_v^0)}{(E - E_v^I)(E - E_c^0)} \right]^{1/2} . \quad (29)$$

Equations (26) and (29) form a system of three equations in the three unknowns, E, k, and λ. In Fig. 3 we present the energy of the conduction state in a quantum dot relative to the bulk crystal conduction-band edge, as a function of radius for the two cases of interest ($l = 0$ and $l = 1$) in the $F = \tfrac{1}{2}$ subspace. These states are twofold degenerate. Parameters have been selected so that the band curvature at the zone center yields an effective mass that is equivalent to the conduction-band effective mass in GaAs ($m_c^* = 0.067m_0$; E_{gap}(GaAs) = 1.424 eV; in addition $m_{LH}^* = 0.082m_0 \approx m_c^*$ indicating that the two-band model is approximately correct). The band-energy constants have been selected to reflect the quantum dot embedded in an $Al_{0.3}Ga_{0.7}As$ barrier ($m_c^* = 0.092m_0$; E_{gap}($Al_{0.3}Ga_{0.7}As$) = 1.798 eV, 60:40 conduction:valence
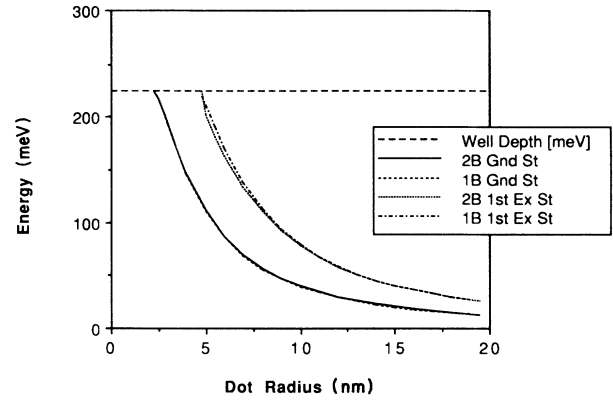

FIG. 3. Confinement energy of the conduction-band states in a spherical GaAs dot embedded in an $Al_{0.3}Ga_{0.7}As$ barrier relative to the bulk GaAs band edge, plotted as a function of dot radius. The ground ("GndSt") and first excited ("1st ExSt") states are shown for both the two-band ("2B") model and the one-band ("1B") model. The dashed line represents the well depth, equal to 224 meV. The difference between the two curves for the first excited state is due to the neglect of band coupling in the one-band model.

energy offset). An important feature of the calculated result is the appearance of a critical quantum dot radius below which no bound states are allowed. This result was previously predicted for quantum dots by solving a simple one band effective-mass Hamiltonian in spherical coordinates.[15]

As a check of the formalism, the above results are com-
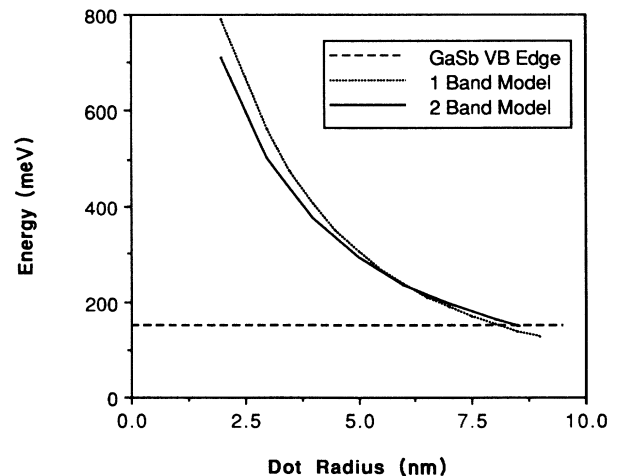
FIG. 4. Confinement energy of the conduction-band states in a spherical InAs dot embedded in a GaSb barrier, plotted as a function of dot radius. The ground state is shown for both the two-band model and the one-band model. The dashed line is the position of the GaSb valence-band edge, 150 meV above the conduction-band edge in bulk InAs. The difference between the two curves is far larger than in Fig. 3 due to the strong band-coupling effects in this type-II structure.

pared in Fig. 3 with a calculation based on a simple one-band effective-mass Hamiltonian. The one-band effective-mass Hamiltonian assumes a parabolic bulk dispersion relation and neglects mixing of the zone-center conduction-band wave function with other bands for nonzero wave numbers. In comparison against the two-band model discussed above, the ground-state energies are in good agreement for all quantum-dot radii. Only in the excited state does a slight difference appear, which becomes more pronounced for stronger confinement (i.e., smaller radii). On the whole, however, the two models agree in this case as we expect.

An extreme situation in which the one-band model would fail for the conduction-band states in a quantum dot is in type-II heterostructures. An InAs dot embedded in GaSb provides an example. In this system, the conduction-band edge of bulk InAs is below the Γ_8 valence-band edge of GaSb. Thus, coupling between the conduction and valence bands across the heterostructure interface cannot be ignored, so that the assumptions underlying the one-band model break down. To determine the conduction-band states in this structure, we employ the two-band formalism that we developed for the GaAs dot. We use the material parameters of Ref. 31 and cal-

culate the position of the lowest conduction band state relative to E_c in InAs as a function of InAs dot radius, in Fig. 4. For comparison we also plot the results calculated using a one-band model of the conduction band in the same figure. It is clear that the two models disagree significantly in this case, by as much as 100 meV for smaller radii, due to the neglect of band-coupling effects in the one-band calculation. We do not extend the calculation beyond the radius at which the InAs conduction state sinks below the GaSb valence-band edge as at this point charge transfer across the surface of the dot may be expected to occur. Quantitative analysis of this interesting effect, which has been observed in InAs/GaSb super-lattices,[32] must incorporate a self-consistent determination of the band bending as in Ref. 33.

We return to the study of type-I systems such as GaAs/Al$_x$Ga$_{1-x}$As, in which the band edges line up closely across the heterostructure, to study the coupled valence-band states in a quantum dot. We first consider states characterized by total angular momentum quantum number $F=\frac{1}{2}$. We neglect the split-off band, retaining only the projection of the Hamiltonian submatrix in this space onto the Γ_8 band edge. As discussed in the Sec. V, the Hamiltonian assumes the form

$$\underline{H}^{\Gamma_8}_{\frac{1}{2},\pm\frac{1}{2}}=\begin{array}{c}|\frac{3}{2},1\rangle \\ |\frac{3}{2},2\rangle\end{array}\begin{array}{cc}|\frac{3}{2},1\rangle & |\frac{3}{2},2\rangle \\ \left[\begin{array}{cc} E_v-(\gamma_1+2\gamma_2)\dfrac{K^2}{2} & 0 \\ 0 & E_v-(\gamma_1+2\gamma_2)\dfrac{K^2}{2}\end{array}\right]\end{array}. \tag{30}$$

The γ's in this matrix are "true" Luttinger parameters. This diagonal matrix contains only light-hole eigenvalues since the $F=\frac{1}{2}$ space contains no heavy-hole character. Because of this decoupling, the vectors $|\frac{3}{2},1\rangle$ and $|\frac{3}{2},2\rangle$ each form quantum-dot bound states with the same energy as that determined in a one-band model of the light holes, corresponding, respectively, to the first and second excited light-hole states. It should be noted, however, that the total wave functions are very different between the coupled band and one-band models. The one-band model of these states predicts a degeneracy of three for $l=1$ and five for $l=2$, plus the twofold spin degeneracy, while the multiple-band calculation yields only the twofold degeneracy in $F_z=\pm\frac{1}{2}$ for the states. As the radial part of the envelopes happens to be the same in the two models, the energy calculation proceeds from this point in a familiar way so we do not pursue it further.

We expect the uppermost valence states (lowest energy in the hole picture) in the spherical quantum dot to have envelopes with a degree of s character, which is not contained in the Γ_8 states spanning the $F=\frac{1}{2}$ space. It is straightforward to show that such states can only appear in the space characterized by total angular momentum $F=\frac{3}{2}$. We consider the submatrix of $\underline{H}_{\frac{3}{2},\pm\frac{3}{2}}$ or $\pm\frac{1}{2}$, Eq. (22), which corresponds to the Γ_8 band edge:

$$\underline{H}^{\Gamma_8}_{\frac{3}{2},\pm\frac{3}{2}\text{ or }\pm\frac{1}{2}}=\begin{array}{c}|\frac{3}{2},0\rangle \\ |\frac{3}{2},2\rangle \\ |\frac{3}{2},1\rangle \\ |\frac{3}{2},3\rangle\end{array}\begin{array}{cccc}|\frac{3}{2},0\rangle & |\frac{3}{2},2\rangle & |\frac{3}{2},1\rangle & |\frac{3}{2},3\rangle \\ \left[\begin{array}{cccc} E_v-\gamma_1\dfrac{K^2}{2} & 2\gamma_2\dfrac{K^2}{2} & 0 & 0 \\ 2\gamma_2\dfrac{K^2}{2} & E_v-\gamma_1\dfrac{K^2}{2} & 0 & 0 \\ 0 & 0 & E_v-(\gamma_1-\frac{8}{5}\gamma_2)\dfrac{K^2}{2} & \frac{6}{5}\gamma_2\dfrac{K^2}{2} \\ 0 & 0 & \frac{6}{5}\gamma_2\dfrac{K^2}{2} & E_v-(\gamma_1+\frac{8}{5}\gamma_2)\dfrac{K^2}{2}\end{array}\right]\end{array}. \tag{31}$$

The matrix is itself block diagonal with the upper-left matrix corresponding to even parity states and the lower right, to odd parity states. For each of the four possible values of F_z ($\pm\frac{3}{2},\pm\frac{1}{2}$) there are, therefore, four eigenvectors: a heavy- and a light-hole eigenvector of each parity

type. The even parity vectors are

$$|\text{LH}\rangle_{\text{even}}=\sqrt{1/2}\{|\frac{3}{2},0\rangle-|\frac{3}{2},2\rangle\}$$

$$|\text{HH}\rangle_{\text{even}}=\sqrt{1/2}\{|\frac{3}{2},0\rangle+|\frac{3}{2},2\rangle\} \tag{32}$$

while the odd parity vectors are given by

$$|\text{LH}\rangle_{\text{odd}} = \tfrac{1}{2}\{|\tfrac{3}{2},1\rangle - 3|\tfrac{3}{2},3\rangle\}$$

$$|\text{HH}\rangle_{\text{odd}} = \tfrac{1}{2}\{3|\tfrac{3}{2},1\rangle + |\tfrac{3}{2},3\rangle\} .$$

(33)

As before, we form these states separately for the regions inside and outside the dot. We then project them onto the radial coordinate of the envelope space. We consider the even parity eigenvectors first. Using Eq. (7), and anticipating the requirement of regularity at the origin, we obtain a two-dimensional column vector for the heavy-hole eigenvector inside the dot in terms of spherical Bessel functions:

$$\phi_E^{\text{HH}}(\rho) = \sqrt{1/2} \begin{bmatrix} j_0(K_{\text{HH}}(E)\rho) \\ j_2(K_{\text{HH}}(E)\rho) \end{bmatrix}$$

(34)

and similarly for the light-hole eigenvector,

$$\phi_E^{\text{LH}}(\rho) = \sqrt{1/2} \begin{bmatrix} j_0(K_{\text{LH}}(E)\rho) \\ -j_2(K_{\text{LH}}(E)\rho) \end{bmatrix} .$$

(35)

Here K_{HH} and K_{LH} are the heavy- and light-hole wave numbers inside corresponding to the dispersion relations: $E_{\text{HH}}(K) = E_v - (\gamma_1 - 2\gamma_2)K^2/2$, and $E_{\text{LH}}(K) = E_v - (\gamma_1 + 2\gamma_2)K^2/2$.

If we assume at this point that the confining potential outside the dot is infinite (an infinite valence-band discontinuity) the total wave function must vanish at the dot surface. Because the radial envelope wave functions are in this case two-component vectors, this boundary condition manifests itself as two independent equations. Thus the quantum-dot eigenstate generally cannot be purely light or heavy-hole in character. The solution must take the form

$$\psi_E = A\phi_E^{\text{HH}}(\rho) + B\phi_E^{\text{LH}}(\rho) .$$

(36)

The requirement that ψ vanish at $\rho = R$ leads to the simple dispersion relation

$$j_0(K_{\text{HH}}(E)R)j_2(K_{\text{LH}}(E)R)$$
$$+ j_0(K_{\text{LH}}(E)R)j_2(K_{\text{HH}}(E)R) = 0 , \quad (37)$$

yielding the valence state eigenenergies E as a function of the dot radius R. Once the energy is known, the constants A and B may be determined, specifying the light- and heavy-hole amplitudes of the state. It is, therefore, in general, qualitatively incorrect to characterize a quantum dot as having light- or heavy-hole states: the quantum-dot confinement potential hybridizes these bands. This effect was recently reported for the infinite-well quantum dot in Ref. 23. We will see below that it is also true for the finite-well case.

The infinite-well-dot eigenstates, which arise from the odd parity block of Eq. (31), are governed by a dispersion relation similar to the one just determined for the even-parity states. Proceeding as we did for the even states, we arrive at the dispersion relation

$$9j_1(K_{\text{HH}}(E)R)j_3(K_{\text{LH}}(E)R)$$
$$+ j_1(K_{\text{LH}}(E)R)j_3(K_{\text{HH}}(E)R) = 0 . \quad (38)$$

For the more realistic case of a dot surrounded by a medium with a finite relative valence-band discontinuity, such as GaAs in $Al_xGa_{1-x}As$, these dispersion relations fail. We must construct a nonvanishing wave function outside the dot. Light- and heavy-hole vectors are formed according to Eqs. (32) and (33) outside the dot. Projecting them upon the envelope-space radial coordinate as before, we obtain expressions similar to Eqs. (34) and (35) except we use spherical Hankel functions to ensure vanishing probability at infinity for the bound states. The wave function inside and outside the dot is then written as a linear combination of the HH and LH vectors in each region, yielding a total of four unknown coefficients. Continuity of the wave function and probability current are required at the interface at radius $\rho = R$ between well and barrier regions, resulting in four equations. The requirement that a solution to this set of equations exist leads to a four-by-four determinental dispersion relation for the allowed eigenenergies. For the even-parity states, this is,

$$\det \begin{vmatrix} j_0(K_{\text{HH}}(E)R) & j_0(K_{\text{LH}}(E)R) & h_0(i\lambda_{\text{HH}}(E)R) & h_0(i\lambda_{\text{LH}}(E)R) \\ j_2(K_{\text{HH}}(E)R) & -j_2(K_{\text{LH}}(E)R) & h_2(i\lambda_{\text{HH}}(E)R) & -h_2(i\lambda_{\text{LH}}(E)R) \\ j_0'(K_{\text{HH}}(E)R) & j_0'(K_{\text{LH}}(E)R) & h_0'(i\lambda_{\text{HH}}(E)R) & h_0'(i\lambda_{\text{LH}}(E)R) \\ j_2'(K_{\text{HH}}(E)R) & -j_2'(K_{\text{LH}}(E)R) & h_2'(i\lambda_{\text{HH}}(E)R) & -h_2'(i\lambda_{\text{LH}}(E)R) \end{vmatrix} = 0 .$$

(39)

In this expression, h is the spherical Hankel function $h^{(1)}$ which decays for imaginary argument. f' denotes derivative of f with respect to ρ, i.e., $f'(kR) = [df(k\rho)/d\rho]|_{\rho=R}$. $K_{\text{LH}}(E)$ and $K_{\text{HH}}(E)$ are defined as before, and $i\lambda_{\text{LH}}(E)$ and $i\lambda_{\text{HH}}(E)$ are the light- and heavy-hole wave numbers outside the dot, taken to be imaginary in anticipation of solving for bound states. A similar dispersion relation follows straightforwardly for the odd-parity states:

$$\det \begin{vmatrix} 3j_1(K_{\text{HH}}(E)R) & j_1(K_{\text{LH}}(E)R) & 3h_1(i\lambda_{\text{HH}}(E)R) & h_1(i\lambda_{\text{LH}}(E)R) \\ j_3(K_{\text{HH}}(E)R) & -3j_3(K_{\text{LH}}(E)R) & h_3(i\lambda_{\text{HH}}(E)R) & -3h_3(i\lambda_{\text{LH}}(E)R) \\ 3j_1'(K_{\text{HH}}(E)R) & j_1'(K_{\text{LH}}(E)R) & 3h_1'(i\lambda_{\text{HH}}(E)R) & h_1'(i\lambda_{\text{LH}}(E)R) \\ j_3'(K_{\text{HH}}(E)R) & -3j_3'(K_{\text{LH}}(E)R) & h_3'(i\lambda_{\text{HH}}(E)R) & -3h_3'(i\lambda_{\text{LH}}(E)R) \end{vmatrix} = 0 .$$

(40)

We have assumed that the effective masses are the same inside and outside the dot for simplicity. Solution of these dispersion relations gives the allowed energies of the quantum dot with a finite-well depth, in the $F=\frac{3}{2}$ spaces.

The highest states calculated with the finite-well quantum-dot dispersion relations are plotted in Fig. 5(a) in the electron picture. The plots reflect a GaAs dot embedded in $Al_{0.3}Ga_{0.7}As$ with a 40% valence-band offset, so the "well depth" is 150 meV. We have assumed $m^*_{LH}=0.082m_0$ and $m^*_{HH}=0.45m_0$. The figure displays the energies of even and odd parity states found with Eqs. (39) and (40) respectively, relative to E_v in bulk GaAs. The state with lowest confinement energy (highest curve in the figure) is of even parity as we expected, while the next is an odd-parity solution. As in the conduction-band calculation, there is a critical radius below which no bound states exist. We point out that each state displayed is fourfold degenerate due to the fourfold degeneracy of $F=\frac{3}{2}$. In Fig. 5(b) we compare the energies of the highest even- and odd-parity states determined using the infinite-well dispersion relations, Eqs. (37) and (38), with the results of the finite-well calculation. The infinite well causes an overestimation of the confinement energy for both states. Note that in the finite well, the energy separation between the even and odd states is enhanced relative to the infinite-well calculation because the odd-parity states has higher probability to be in the barrier region than the even state. Thus the infinite-well model yields energies for these states that are inaccurate both qualitatively as well as quantitatively.

The results of a one-band calculation for the heavy- and light-hole states in a GaAs quantum dot surrounded by $Al_{0.3}Ga_{0.7}As$, using the same material parameters as in our multiple-band calculation, are shown in Fig. 5(c) for comparison to the coupled band model used in Fig. 5(a). Note the level crossings which occur in the one-band model do not occur when band coupling effects are included. Furthermore, the highest state in our multiple-band calculation is significantly lower than the highest heavy-hole state in the one-band model. This is due to the fact that the dot eigenstates are an admixture of light- and heavy-hole character. Any admixture of lower mass light-hole character into the heavy-hole ground state would naturally tend to increase the confinement energy, pushing it downwards on the energy scale of Fig. 5(c).

This admixture has a significant impact on the electrical properties and optical spectra of these structures, and hence must be taken into account if applications involving quantum dots, such as to semiconductor lasers, are to be accurately studied. Information about the optical properties of the quantum dot may be straightforwardly obtained by using the dot eigenstates, such as Eq. (36) for the valence bands, to calculate matrix elements for optical transitions between conduction- and valence-band states. A calculation of the optical matrix element between the lowest conduction- and highest valence-band states shows that this transition in the quantum dot is optically isotropic, as we expect in a spherical band-structure approximation.[1] This result could not be obtained in a one-band model. We mention that all of the
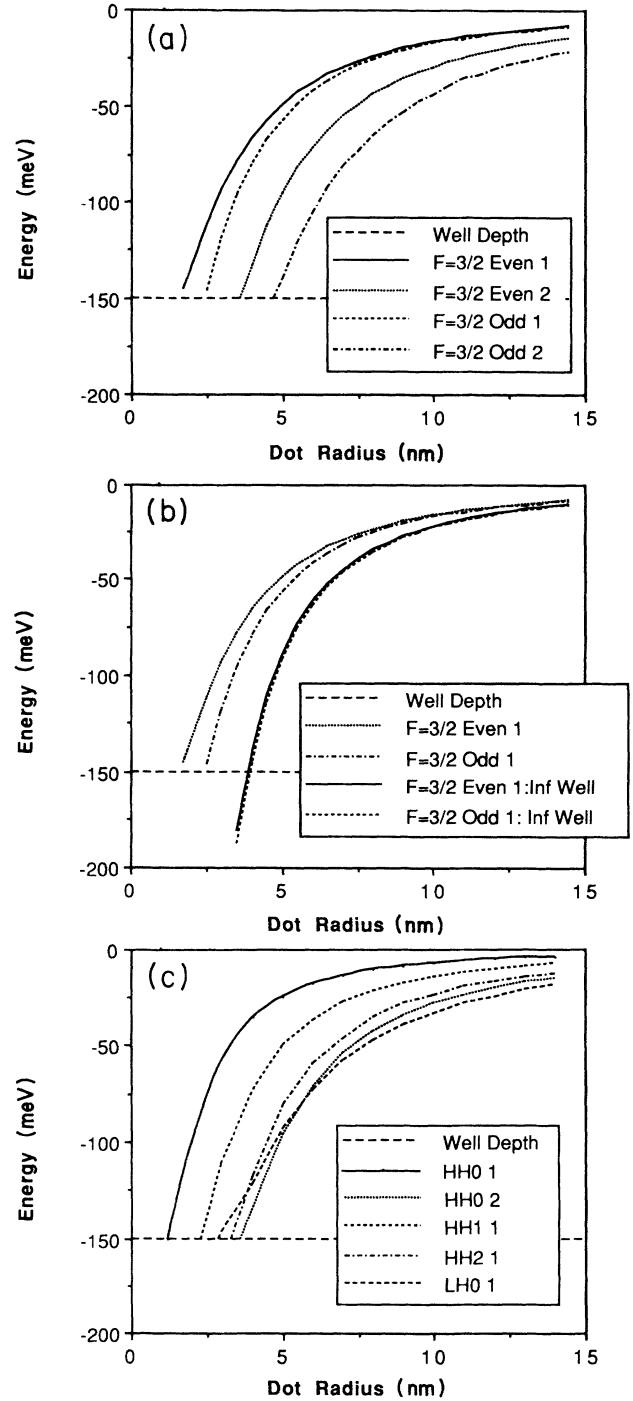
FIG. 5. Confinement energy of bound valence-band states in a spherical GaAs quantum dot plotted vs dot radius, relative to E_v in bulk GaAs. The dot is embedded in an $Al_{0.3}Ga_{0.7}As$ barrier, reflected in a well depth of 150 meV. (a) Coupled band model of the light and heavy holes. The states belong to the $F=\frac{3}{2}$ space and are labeled according to parity (even or odd) and order in energy (1,2, ... ,). (b) A comparison of the finite- and infinite-well models. Note that in the finite well the energy of the odd state is substantially below that of the even state, while the two are nearly degenerate for the infinite well. (c) A one-band calculation. Effective masses are the same as in Fig. 5(a). The states are identified by the band (HH or LH), the envelope angular momentum and order in energy. Note the level crossings, which do not occur in the coupled band model.

calculations presented in this paper were performed either analytically, or where necessary, on a desk top personal computer, implying that incorporation of band-coupling effects into device analyses is simple and therefore warranted. We next turn our attention to the quantum wire.

VI. BAND STRUCTURE IN A CYLINDRICAL REPRESENTATION

Our success in solving the multiple-band quantum-dot problem arose from the compatibility of the total angular momentum F with the band-structure Hamiltonian in the spherical approximation. A similar simplification applies in the case of the quantum wire. In contrast to the spherical case, where we used the complete set of commuting observables including H, $\mathbf{F}^2$, and F_z, we now a use a basis of eigenstates shared by H, F_z, and P_z, the component of envelope linear momentum along the z axis. This basis has the desired symmetry for studying the cylindrical quantum wire. F_z is a good quantum number so the Hamiltonian in this basis is again block diagonal

$$\underline{H} = \sum_{F_z} \underline{H}_{F_z} . \tag{41}$$

In contrast to the approach in Sec. IV for the spherically symmetric problem, it is most convenient to work in an "uncoupled" angular momentum representation. We use the fact that $F_z = J_z + L_z$ to construct a basis in the product form

$$|K_z, k, F_z; J, J_z\rangle = |J, J_z\rangle |K_z; k, L_z = F_z - J_z\rangle . \tag{42}$$

The envelope vector $|K_z; k, L_z\rangle$, described below, is an eigenstate of L_z, the projection of envelope angular momentum along the z axis with quantum number L_z. The zone-center Bloch function $|J, J_z\rangle$, as before, has Bloch angular momentum quantum numbers J, J_z. The envelope vectors are simultaneously eigenstates of P_z, the z component of the envelope momentum operator, with eigenvalue $\hbar K_z$. The envelope states, therefore, have the cylindrical coordinate representation

$$\langle r, \theta, z | K_z; k, L_z\rangle = \frac{i^{L_z}}{2\pi} H_{L_z}(kr) e^{iL_z\theta} e^{iK_z z} , \tag{43}$$

where k is a radial wave number and H is a Hankel function. It is clear that the resulting basis has the necessary cylindrical symmetry. It is also an orthonormal basis

$$\langle K_z', k', F_z'; J', J_z' | K_z, k, F_z; J, J_z\rangle$$
$$= \delta_{F_z', F_z} \delta_{J', J} \delta_{J_z', J_z} \frac{\delta(k'-k)}{k} \delta(k_z'-k_z) . \tag{44}$$

The process of expressing the band-structure Hamiltonian in this basis involves a unitary transformation similar to that carried out in the spherical case. It is simple to show that the transformation from the conventional Bloch plane-wave basis into the new cylindrical wave basis is

$$\langle K_z, k, F_z; J, J_z | \psi\rangle = \int d\theta_{\mathbf{K}'} e^{-i(F_z - J_z)\theta_{\mathbf{K}'}} \langle \mathbf{K}'; J, J_z | \psi\rangle . \tag{45}$$

In this equation, $\langle \mathbf{K}'; J, J_z | \psi\rangle$ are the components of a wave function ψ written in the conventional basis of

TABLE II. Cylindrical representation for the subblock $\underline{H}_{F_z}$ of the Hamiltonian. The symbols are defined in the text. This matrix represents coupling among conduction, light and heavy hole, and split-off bands, including indirect coupling through remote bands.

Bloch plane waves. $\theta_{K'}$ is the angular coordinate of the vector K' expressed in cylindrical coordinates. Using this unitary transformation we find the matrix elements of the band-structure Hamiltonian in the new basis in terms of the conventional matrix elements (found in the Appendix):

$$\langle K_z, k, F_z'; J', J_z' | H | K_z, k, F_z; J, J_z \rangle$$

$$= \frac{1}{2\pi} \int_0^{2\pi} d\theta_K \, e^{i[(F_z - F_z') - (J_z - J_z')]\theta_K}$$

$$\times \langle K; J', J_z' | H | K; J, J_z \rangle \,. \quad (46)$$

Employing this transformation equation, we find that each Hamiltonian subblock $\underline{H}_{F_z}$ [see (41)] assumes the identical 8×8 form given in Table II. This is the full Hamiltonian governing conduction, light and heavy holes, and the split-off bands. In the table, the basis vectors are written as products of a zone-center Bloch function, $|J, J_z\rangle$ and an envelope state, $|F_z - J_z\rangle$ so that $L_z = F_z - J_z$. This form ensures that all the basis vectors correspond to the same quantum number F_z. In the envelope vector, k and K_z are understood and therefore omitted. P is the Kane matrix element. The other terms are given by

$$-\frac{T}{2} = (\gamma_1 + \gamma_2)\frac{k^2}{2} + (\gamma_1 - 2\gamma_2)\frac{K_z^2}{2}, \quad -\left[\frac{T}{6} + \frac{2Q}{3}\right] = (\gamma_1 - \gamma_2)\frac{k^2}{2} + (\gamma_1 + 2\gamma_2)\frac{K_z^2}{2} \,,$$

$$(47)$$

$$-L = \begin{cases} -i2\sqrt{3}\gamma_3 \dfrac{kK_z}{2} & \text{(axial approximation)} \\[2ex] -i2\sqrt{3}\gamma_2 \dfrac{kK_z}{2} & \text{(spherical approximation)}, \end{cases} \qquad -M = \sqrt{3}\gamma_2 \dfrac{k^2}{2} \,.$$

These subblocks are quite similar in structure to the conventional Cartesian coordinate Hamiltonian (see the Appendix), but K_x and K_y are everywhere replaced by the radial wave number, k. Either the spherical or the axial approximation may be employed as indicated in the expression for the term L. In the more accurate axial approximation, we equate γ_2 and γ_3 only in the term M, so that warping effects are neglected only in the (K_x, K_y) plane. Thus the energy bands remain cylindrically symmetric about the quantization axis and F_z remains conserved. The axial approximation is, therefore, naturally incorporated into the present formalism, in contrast to coordinate free methods which have been previously applied to the cylindrical quantum wire.[22] It is easily shown that the band-structure relations, which result from diagonalizing these submatrices, agree with those obtained via the conventional K·P method using the same approximations. However, the eigenvectors have cylindrical symmetry, so that the cylindrical quantum-wire problem is now easily solved by the same algebraic method that we used for the spherical quantum dot.

VII. ELECTRONIC STRUCTURE OF THE CYLINDRICAL QUANTUM WIRE

By treating the band-structure parameters such as E_c and E_v as functions of the radial coordinate in the Hamiltonian given in Table I, we can model the cylindrical wire heterostructure just as in the case of the quantum dot. We find that the one-band model is adequate for conduction-band states in systems like GaAs/Al$_x$Ga$_{1-x}$As, but fails in the case of type-II systems such as InAs/GaSb.

We narrow our focus now to the more interesting Γ_8 states—the light and heavy holes—and calculate the quantum wire subband dispersion relations $E(K_z)$ for these bands. For the light and heavy holes, we retain only the middle 4×4 block of the Hamiltonian in Table II, incorporating the effects of coupling to the conduction and split-off bands through the Luttinger parameters in the spherical approximation:

	$\|\frac{3}{2},\frac{3}{2}\rangle\|F_z-\frac{3}{2}\rangle$	$\|\frac{3}{2},\frac{1}{2}\rangle\|F_z-\frac{1}{2}\rangle$	$\|\frac{3}{2},-\frac{1}{2}\rangle\|F_z+\frac{1}{2}\rangle$	$\|\frac{3}{2},-\frac{3}{2}\rangle\|F_z+\frac{3}{2}\rangle$	
$H_{F_z}^{\Gamma_8} = $	$E_v + T_2$	$-iL$	$-M$	0	
	iL^*	$E_v + \dfrac{T}{6} + \frac{2}{3}Q$	0	$-M$	(48)
	$-M^*$	0	$E_v + \dfrac{T}{6} + \frac{2}{3}Q$	iL	
	0	$-M^*$	$-iL^*$	$E_v + \dfrac{T}{2}$	

For a given F_2, the heavy and light holes each have two eigenvectors. The heavy-hole vectors are

$$|HH\rangle_1 = \begin{bmatrix} \dfrac{1}{\sqrt{3}}\dfrac{k^2+4K_z^2}{k^2} \\[2mm] \dfrac{2K_z}{k} \\[2mm] 1 \\[2mm] 0 \end{bmatrix}, \quad |HH\rangle_2 = \begin{bmatrix} \dfrac{2K_z}{k} \\[2mm] \sqrt{3} \\[2mm] 0 \\[2mm] 1 \end{bmatrix}, \quad (49)$$

where the heavy-hole eigenvalue is $E_{HH}(k)=E_v-(\gamma_1-2\gamma_2)(k^2+K_z^2)/2$. The light-hole vectors are

$$|LH\rangle_1 = \begin{bmatrix} -\sqrt{3} \\[2mm] \dfrac{2K_z}{k} \\[2mm] 1 \\[2mm] 0 \end{bmatrix}, \quad |LH\rangle_2 = \begin{bmatrix} \dfrac{2K_z}{k} \\[2mm] -\dfrac{1}{\sqrt{3}}\dfrac{k^2+4K_z^2}{k^2} \\[2mm] 0 \\[2mm] 1 \end{bmatrix}, \quad (50)$$

with eigenvalue $E_{LH}(k)=E_v-(\gamma_1+2\gamma_2)(k^2+K_z^2)/2$. Note that if $K_z=0$ the Γ_8 Hamiltonian, Eq. (48), decouples into two 2×2 blocks of even or odd parity. The vectors subscripts 1 and 2 will then contain separately envelopes of either purely even- or purely odd-parity, depending on F_z. Thus, by taking the quantum-wire axis to be the quantization direction, we not only obtain a simple radial boundary condition for the wave functions of the quantum wire, but also a significant simplication in determining subband-edge $(K_z=0)$ wave functions and energies. This is pointed out because the optical properties of the quantum wire will be dominated by the subband-edge states.

As in the quantum-dot calculation, we treat the band-structure parameters as a function of the cylindrical radial coordinate r, form heavy- and light-hole vectors separately inside and outside the quantum wire, and project them onto the envelope space radial coordinate. Inside the wire, the envelopes must be regular so these projections are

$$\phi_{F_z}^{HH1}(r,z) = \begin{bmatrix} \dfrac{1}{\sqrt{3}}\dfrac{k^2+4K_z^2}{k^2}J_{F_z-\frac{3}{2}}(k_{HH}(E)r) \\[2mm] \dfrac{2K_z}{k}J_{F_z-\frac{1}{2}}(k_{HH}(E)r) \\[2mm] J_{F_z+\frac{1}{2}}(k_{HH}(E)r) \\[2mm] 0 \end{bmatrix}\exp(iK_z z), \quad \phi_{F_z}^{HH2}(r,z) = \begin{bmatrix} \dfrac{2K_z}{k}J_{F_z-\frac{3}{2}}(k_{HH}(E)r) \\[2mm] \sqrt{3}J_{F_z-\frac{1}{2}}(k_{HH}(E)r) \\[2mm] 0 \\[2mm] J_{F_z+\frac{3}{2}}(k_{HH}(E)r) \end{bmatrix}\exp(iK_z z), \quad (51)$$

and

$$\phi_{F_z}^{LH1}(r,z) = \begin{bmatrix} -\sqrt{3}J_{F_z-\frac{3}{2}}(k_{LH}(E)r) \\[2mm] \dfrac{2K_z}{k}J_{F_z-\frac{1}{2}}(k_{LH}(E)r) \\[2mm] J_{F_z+\frac{1}{2}}(k_{LH}(E)r) \\[2mm] 0 \end{bmatrix}\exp(iK_z z), \quad \phi_{F_z}^{LH2}(r) = \begin{bmatrix} \dfrac{2K_z}{k}J_{F_z-\frac{3}{2}}(k_{LH}(E)r) \\[2mm] -\dfrac{1}{\sqrt{3}}\dfrac{k^2+4K_z^2}{k^2}J_{F_z-\frac{1}{2}}(k_{LH}(E)r) \\[2mm] 0 \\[2mm] J_{F_z+\frac{3}{2}}(k_{LH}(E)r) \end{bmatrix}\exp(iK_z z). \quad (52)$$

For bound states, the wave functions outside the wire must be normalizable, so the projections in the barrier region involve Hankel functions $H^{(1)}$ in place of the Bessel functions J appearing in the expressions above.

The quantum-wire eigenstates are then formed in each region as a superposition of the bulk light and heavy-hole vectors. If we specialize for the moment to the case of a quantum wire with an infinite-well depth, the boundary condition is that the wave function inside must vanish at the surface of the wire, $r=R$. Since the states are four-component vectors, this requirement can be satisfied generally only if the wave function is a superposition of the four bulk light- and heavy-hole eigenstates for a given F_z, such as

$$\psi_{F_z}(E) = A|HH\rangle_1 + B|HH\rangle_2 + C|LH\rangle_1 + E|LH\rangle_2 . \quad (53)$$

By forcing this state to vanish at R, we obtain a 4×4 determinantal dispersion relation giving the allowed energies for the infinite-well quantum wire, namely

$$\det \begin{vmatrix} \dfrac{1}{\sqrt{3}}\dfrac{k_{HH}^2+4K_z^2}{k_{HH}^2}J_{F_z-\frac{3}{2}}(k_{HH}R) & \dfrac{2K_z}{k_{HH}}J_{F_z-\frac{3}{2}}(k_{HH}R) & -\sqrt{3}J_{F_z-\frac{3}{2}}(k_{LH}R) & \dfrac{2K_z}{k_{LH}}J_{F_z-\frac{3}{2}}(k_{KH}R) \\[3mm] \dfrac{2K_z}{k_{HH}}J_{F_z-\frac{1}{2}}(k_{HH}R) & \sqrt{3}J_{F_z-\frac{1}{2}}(k_{HH}R) & \dfrac{2K_z}{k_{LH}}J_{F_z-\frac{1}{2}}(k_{LH}R) & -\dfrac{1}{\sqrt{3}}\dfrac{k_{LH}^2+4K_z^2}{k_{LH}^2}J_{F_z-\frac{1}{2}}(k_{LH}R) \\[3mm] J_{F_z+\frac{1}{2}}(k_{HH}R) & 0 & J_{F_z+\frac{1}{2}}(k_{LH}R) & 0 \\[3mm] 0 & J_{F_z+\frac{3}{2}}(k_{HH}R) & 0 & J_{F_z+\frac{3}{2}}(k_{LH}R) \end{vmatrix} = 0 . \quad (54)$$

This dispersion relation is equivalent to the one reported in Ref. 22, which was derived using a coordinate free form for the Luttinger Hamiltonian. The formalism presented in this work is more general in that explicit coupling to the conduction and split-off bands is incorporated into the general Hamiltonian. The formalism reduces to that presented in Ref. 22 for the case of the isolated Γ_8 states we are presently calculating.

Before returning to the finite-well problem, we stop to examine some qualitative features which become apparent in the steps leading to the infinite-well dispersion relation. The only possibility for the light and heavy holes to decouple in the wire exists in the spaces corresponding to $F_z = \pm\frac{1}{2}$ at the zone center ($K_z = 0$) where parity is a good quantum number. In this case, the odd-parity vectors in Eq. (51) and (52) have two nonzero envelope components, proportional to $J_{\pm 1}(kr)$. Since $J_{-1}(x) = -J_1(x)$, the infinite-well boundary condition at the wire interface is equivalent to just one equation: $J_1(kr) = 0$. Thus the light- and heavy-hole vectors decouple in this specific case, and the corresponding subband-edge energies are identical to those predicted by a one-band model. However, for the even-parity vectors corresponding to $F_z = \pm\frac{1}{2}$, and for all other zone-center vectors, both even and odd, with $|F_z| > \frac{1}{2}$, the indices of the Bessel functions for the two nonzero components are not equal. As a result, light- and heavy-hole waves must be mixed to satisfy the boundary conditions at the wire interface, and the one-band model fails even to predict correct subband-edge energies. The quantum-wire eigenstates are, therefore, in general, hybrids of light- and heavy-hole character, even at the zone center. With

nonzero K_z this mixing further increases. This effect, which has been reported for wires of square cross section,[12,14] in addition to the cylindrical wire result reported here, is in distinct contrast to the situation in the conventional planar quantum well, in which light- and heavy-hole states are always decoupled at the zone center. It is therefore not possible to label quantum-wire subbands as light or heavy hole in character as is done in the quantum well.

This remains true for the finite-well quantum wire. To solve this problem, we must construct states in the barrier region in addition to the states inside the wire. As indicated above, the barrier states contain Hankel functions which decay as r increases to infinity. The quantum-wire eigenstates in the well and in the barrier are formed separately as superpositions of the two light- and two heavy-hole vectors in the respective regions, leaving four constants in the well and four constants in the barrier to be determined. By requiring continuity of the wave functions (four equations) and the probability current (four more equations) across the interface between well and barrier regions, we obtain an 8×8 determinantal dispersion relation which determines the allowed quantum-wire eigenenergies and eigenstates. We take the effective-mass parameters to be the same in the well and barrier, and write this dispersion relation in the compact form:

$$\det \begin{vmatrix} \underline{\Phi}_{\text{inside}} & \underline{\Phi}_{\text{outside}} \\ \underline{\Phi}'_{\text{inside}} & \underline{\Phi}'_{\text{outside}} \end{vmatrix} = 0 \tag{55}$$

where the $\underline{\Phi}$ are 4×4 blocks given by

$$\underline{\Phi}_{\text{inside}} = \begin{bmatrix} \dfrac{1}{\sqrt{3}} \dfrac{k_{\text{HH}}^2 + 4K_z^2}{k_{\text{HH}}^2} J_{F_z - \frac{3}{2}}(k_{\text{HH}}R) & \dfrac{2K_z}{k_{\text{HH}}} J_{F_z - \frac{3}{2}}(k_{\text{HH}}R) & -\sqrt{3} J_{F_z - \frac{3}{2}}(k_{\text{LH}}R) & \dfrac{2K_z}{k_{\text{LH}}} J_{F_z - \frac{3}{2}}(k_{\text{LH}}R) \\ \dfrac{2K_z}{k_{\text{HH}}} J_{F_z - \frac{1}{2}}(k_{\text{HH}}R) & \sqrt{3} J_{F_z - \frac{1}{2}}(k_{\text{HH}}R) & \dfrac{2K_z}{k_{\text{LH}}} J_{F_z - \frac{1}{2}}(k_{\text{LH}}R) & -\dfrac{1}{\sqrt{3}} \dfrac{k_{\text{LH}}^2 + 4K_z^2}{k_{\text{LH}}^2} J_{F_z - \frac{1}{2}}(k_{\text{LH}}R) \\ J_{F_z + \frac{1}{2}}(k_{\text{HH}}R) & 0 & J_{F_z + \frac{1}{2}}(k_{\text{LH}}R) & 0 \\ 0 & J_{F_z + \frac{3}{2}}(k_{\text{HH}}R) & 0 & J_{F_z + \frac{3}{2}}(k_{\text{LH}}R) \end{bmatrix} \tag{56}$$

and

$$\underline{\Phi}_{\text{outside}} = \begin{bmatrix} \dfrac{1}{\sqrt{3}} \dfrac{\kappa_{\text{HH}}^2 + 4K_z^2}{\kappa_{\text{HH}}^2} H_{F_z - \frac{3}{2}}(\kappa_{\text{HH}}R) & \dfrac{2K_z}{\kappa_{\text{HH}}} H_{F_z - \frac{3}{2}}(\kappa_{\text{HH}}R) & -\sqrt{3} H_{F_z - \frac{3}{2}}(\kappa_{\text{LH}}R) & \dfrac{2K_z}{\kappa_{\text{LH}}} H_{F_z - \frac{3}{2}}(\kappa_{\text{LH}}R) \\ \dfrac{2K_z}{\kappa_{\text{HH}}} H_{F_z - \frac{1}{2}}(\kappa_{\text{HH}}R) & \sqrt{3} H_{F_z - \frac{1}{2}}(\kappa_{\text{HH}}R) & \dfrac{2K_z}{\kappa_{\text{LH}}} H_{F_z - \frac{1}{2}}(\kappa_{\text{LH}}R) & -\dfrac{1}{\sqrt{3}} \dfrac{\kappa_{\text{LH}}^2 + 4K_z^2}{\kappa_{\text{LH}}^2} H_{F_z - \frac{1}{2}}(\kappa_{\text{LH}}R) \\ H_{F_z + \frac{1}{2}}(\kappa_{\text{HH}}R) & 0 & H_{F_z + \frac{1}{2}}(\kappa_{\text{LH}}R) & 0 \\ 0 & H_{F_z + \frac{3}{2}}(\kappa_{\text{HH}}R) & 0 & H_{F_z + \frac{3}{2}}(\kappa_{\text{LH}}R) \end{bmatrix} \tag{57}$$

and each term in the blocks labeled Φ' is the derivative with respect to r of the corresponding term in Φ. k_{HH} and k_{LH} are the wave numbers corresponding to $E(k) = E_v - (\gamma_1 \mp 2\gamma_2)(k^2 + K_z^2)/2$, where the minus applies to the heavy holes and the plus to the light holes. κ_{HH} and κ_{LH} are similarly defined in the barrier.

We have solved this dispersion relation for a GaAs wire embedded in an $\text{Al}_{0.3}\text{Ga}_{0.7}\text{As}$ barrier region for

several wire radii, using the same band-structure parameters as in Sec. V. We begin by presenting plots of the subband-edge ($K_z = 0$) energies of bound states as a function of wire radius. Figure 6(a) shows edge energies for all of the bound subbands corresponding to $F_z = \pm\frac{1}{2}$ for radii up to $R = 10$ nm, relative to E_v in GaAs. Figures 6(b) and 6(c) similarly show the bound subband edges in $F_z = \pm\frac{3}{2}$ and $F_z = \pm\frac{5}{2}$, respectively. The states are labeled

according to parity in Figs. 6(a)–6(c) since at the quantum-wire zone center, parity is a good quantum number. In Fig. 6(d) we show the position of the four highest subband edges versus wire radius calculated in a one-band model for heavy and light holes using the same band-structure parameters as for the coupled band calculations. A comparison of these plots shows the effect of the admixture of light- and heavy-hole character in the zone-center quantum-wire states, discussed above. The highest state in Fig. 6(a) is substantially lower for all radii than the HH0 state in the one-band model, reflecting admixture of light-hole character into the wave function. The confinement energies increase as we decrease wire radius, as expected. Also, confinement energies for a given radius tend to be larger for states of higher F_z. The highest subband (lowest confinement energy) corresponds to an even-parity state with $F_z = \pm \frac{1}{2}$. Note that, in contrast to the situation in the quantum dot, there is always at least one bound state in the wire, though as r approaches zero the subband edge of the states approaches the top of the well asymptotically. This point was first pointed out for the one-band case in Ref. 16.

In Figures 7(a) and 7(b) we show the subband dispersion, $E(K_z)$ for bound states corresponding to $F_z = \pm \frac{1}{2}$ and $F_z = \pm \frac{3}{2}$, respectively, in a GaAs/Al$_{0.3}$Ga$_{0.7}$As quantum wire with radius 5 nm. Reference to Fig. 6(c) shows that there are no bound states for the 5 nm radius wire in the spaces $F_z = \pm \frac{5}{2}$: Figures 7(a) and 7(b) represent all bound states for this radius. These plots were made by solving Eq. (55) numerically on a desk top personal computer. The states are labeled according to the parity of the zone-center envelope wave function. The strong nonparabolicity of the subband structure is a result of the no-crossing rule for coupled states, reflecting the importance of band-coupling effects in this system. The most extreme result of this coupling is seen in Fig. 7(b), in which the highest subband is actually electronlike at zone center. Similar effects manifest themselves in Figs. 8(a) and 8(b), which show the dispersion of the bound subbands in a wire of radius 2.5 nm. Reference to Figs. 6(a)–6(c) shows that these plots describe all bound states for this radius.

It is instructive to examine the effective masses at the subband edges as a function of wire radius. We have
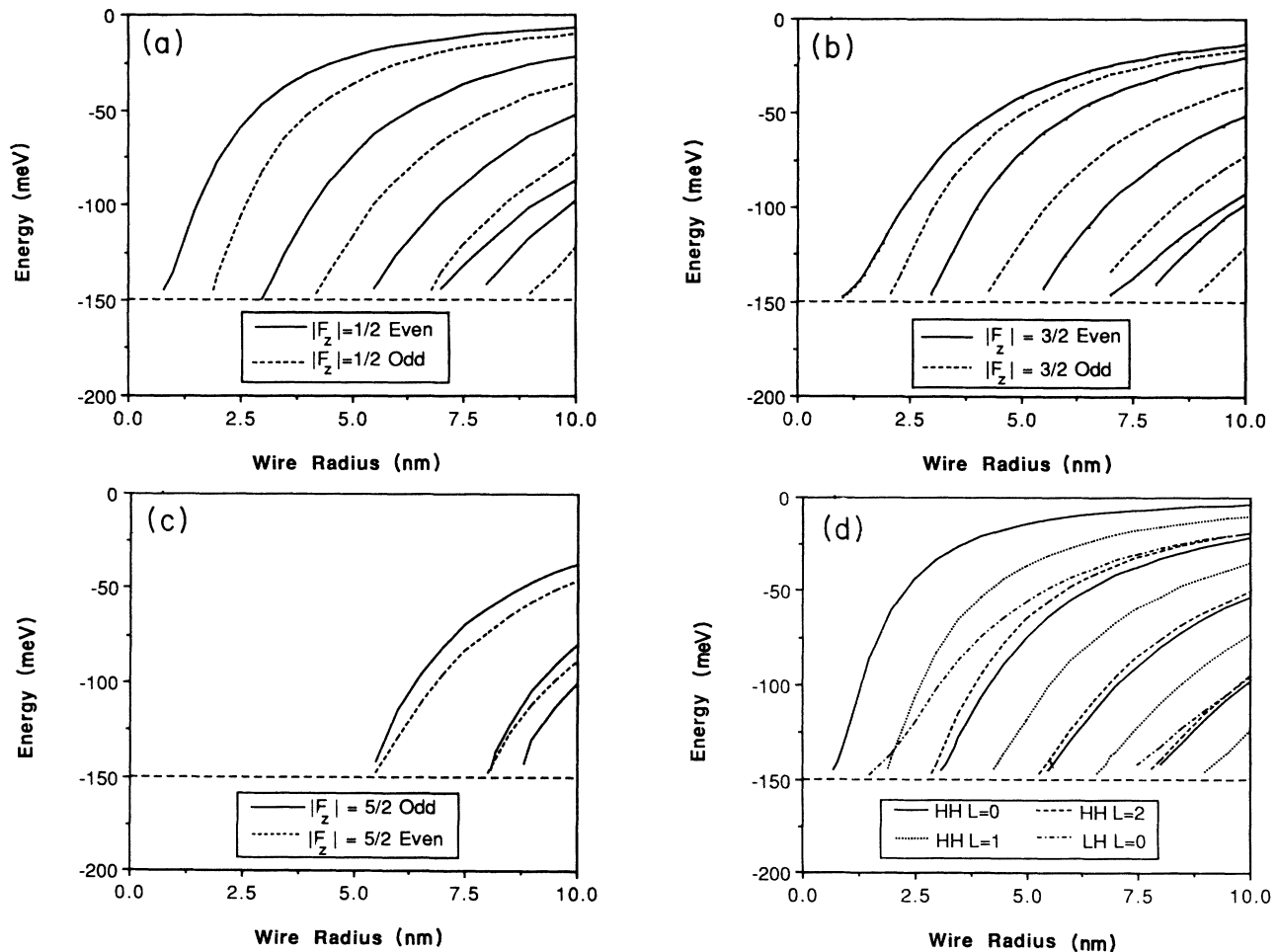

FIG. 6. Confinement energy at the zone center ($K_z = 0$) for bound valence-band states in a cylindrical GaAs quantum wire embedded in an Al$_{0.3}$Ga$_{0.7}$As barrier (well depth = 150 meV) plotted versus wire radius. (a) Coupled band model, $F_z = \pm \frac{1}{2}$. The states are labeled according to their parity, which is a good quantum number at zone center. (b) Coupled band model, $F_z = \pm \frac{3}{2}$. (c) Coupled band model, $F_z = \pm \frac{5}{2}$. (d) One-band model with the same effective masses as in (a)–(c). The states are identified by the band (HH or LH) and the quantum number L_z.

determined these masses by performing a quadratic best fit to the subband dispersion curves near the subband edges, as in Ref. 13. The results for the highest subband, for both infinite- and finite-well depths, are shown in Table III. The mass is as low as $0.16m_0$ for the 2.5 nm radius wire with finite-well depth, and increases somewhat with increasing wire radius. In the approximation of an infinitely deep well, the mass is found to be $m^* = 0.25m_0$, independent of wire radius. A similar result was reported for a quantum wire of square cross section in the infinite-well approximation, in Ref. 13. However, in that study, the mass of the highest valence subband was found to be $m^* = 0.027m_0$, nearly ten times lighter than our value for the infinite-well case. This discrepancy is explained by the fact that the light- and heavy-hole states are assumed to decouple at the quantum-wire zone center in Ref. 13, an assumption which has been shown here to be invalid, as well as in previous studies by other workers.[12,14,22]

The effective mass of the highest valence subband in a quantum wire of a given diameter tends to be heavier than that for the corresponding state in a planar quantum well with a comparable thickness. This is best seen in the
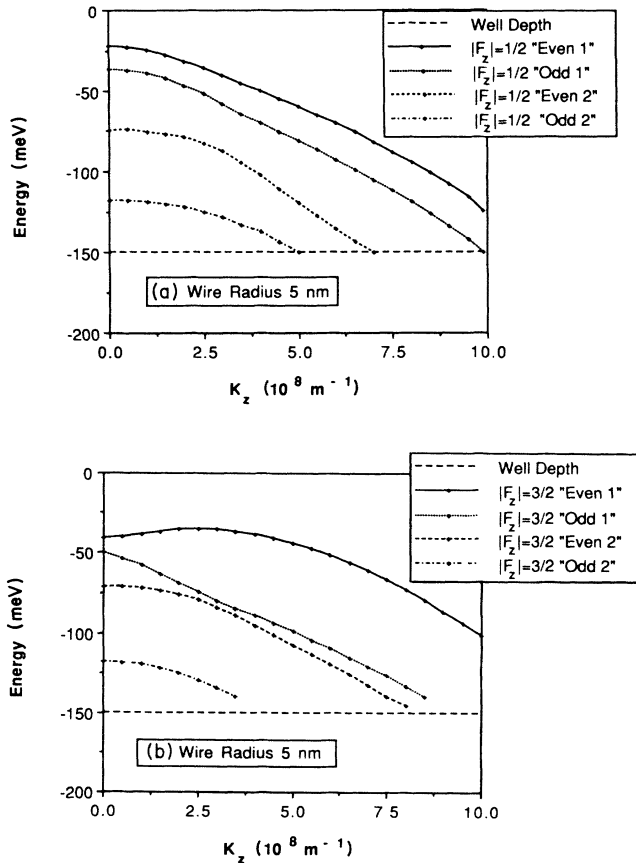

FIG. 7. Subband dispersion $E(K_z)$ for a 5 nm radius GaAs quantum wire embedded in an $Al_{0.3}Ga_{0.7}As$ barrier (well depth = 150 meV). (a) $F_z = \pm\frac{1}{2}$. The dispersion curves are labeled according to the parity of the zone-center state to which they correspond. (b) $F_z = \pm\frac{3}{2}$. Note that the highest state in this space is electronlike near the subband edge.
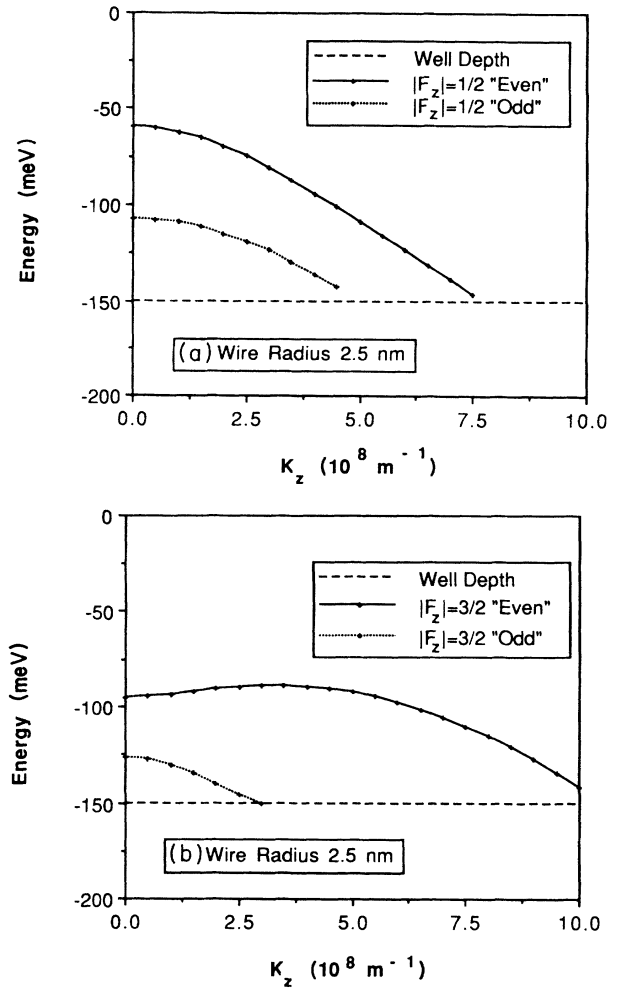

FIG. 8. Subband dispersion $E(K_z)$ for a 2.5 nm radius GaAs quantum wire embedded in an $Al_{0.3}Ga_{0.7}As$ barrier (well depth = 150 meV). (a) $F_z = \pm\frac{1}{2}$. (b) $F_z = \pm\frac{3}{2}$. See comments in Fig. 7.

approximation of infinite-well depth. In this approximation, the mass of the highest valence subband in a GaAs quantum well is $m^* = 0.118m_0$, independent of well thickness,[11] in contrast to $m^* = 0.25m_0$ for the highest quantum-wire subband. The valence subbands in a quantum wire tend to be more numerous and therefore more closely spaced in energy than in a quantum well with comparable thickness due to the additional confinement and band-coupling effects in the wire structure. (This rather counter-intuitive effect is *not* true in a simple-one-band model in which band coupling is neglected.) This is

TABLE III. Effective mass at the subband edge of the highest subband in a GaAs quantum wire embedded in an $Al_{0.3}Ga_{0.7}As$ barrier, for several wire radii. Also included in the table are values determined in the approximation of infinite-well depth.

Quantum wire well depth	Radius		
	2.5 nm	5 nm	10 nm
Infinite	$0.25m_0$	$0.25m_0$	$0.25m_0$
150 meV	$0.16m_0$	$0.19m_0$	$0.27m_0$

TABLE IV. A comparison of the effective mass for valence-band in-plane dispersion in a GaAs quantum well and down-wire dispersion in a quantum wire. The values are calculated in the approximation of an infinite-well depth. The quantum-well state labeled HH1 is heavy-hole-like with even parity at the subband edge. $\Delta E_{2,1}$ is the energy separation between HH1 and HH2, the next highest state, which has odd parity. Corresponding values are given for the highest even- and odd-parity states for the quantum wire, which have quantum number $F_z = \pm\frac{1}{2}$. The larger energy separation between HH1 and HH2 implies a lighter effective mass in the quantum well.

State	E (meV)	$\Delta E_{2,1}$ (meV)	m^*/m_0
Well: HH1	-8.3	24.9	0.118
Wire: $F_z = \frac{1}{2}$ even 1	-39.6	9.8	0.250

seen in Table IV. There, the edge energy of the highest valence subband (HH1) in an infinitely deep quantum well of thickness 10 nm is listed, with the energy separation to the next state (HH2) and the effective mass for in-plane dispersion. The corresponding parameters are given for the highest valence state of a 10 nm diameter quantum wire with infinite-well depth (which belongs to the $F_z = \pm\frac{1}{2}$ subspace). The energy separation to the second highest state is lower in the quantum wire than in the planar well by over a factor of 2. As a result, the coupling between these levels is stronger in the wire, causing the higher subband to "flatten out" due to the no-crossing rule. This is reflected in the mass—it is more than two times higher in the wire than in the well.

A more comprehensive study of the subband structure and effective masses in a cylindrical quantum wire will appear elsewhere, incorporating band-warping effects into the calculation by employing the axial approximation discussed in Sec. VII.[34] In the axial approximation, actual band structure in a cubic semiconductor is more accurately reproduced than in the spherical approximation, yet, since F_z remains a good quantum number, the calculation is only moderately more complicated.

Finally, we point out that it is straightforward to obtain exact, closed-form expressions for the quantum-wire wave functions using the formalism we have presented. This is necessary for studying such important topics as excitons in the quantum wire, and matrix elements for optical transitions. The band coupling has a profound effect on these calculations and must not be ignored if realistic results are to be obtained. For example, a calculation of the lowest energy optical transition in the cylindrical quantum wire shows that the square of the optical matrix element is four times larger when the electric field vector is oriented along the wire than for the perpendicular orientation.[1] This result could not be obtained using a simple one-band model.

VIII. CONCLUSIONS

We have demonstrated an analytical formalism for studying band structure in quantum dots and quantum wires. The technique is based upon the critical observation that the envelope-function approximation is equivalent to a two-particle model of the electrons in a semiconductor. In the spherical approximation, the band-structure Hamiltonian commutes with the sum of the angular momenta of these particles, which we term Bloch and envelope. The total angular momentum **F** therefore, provides good quantum numbers in centrosymmetric systems, a general result originally found in the context of the acceptor problem. Application of the theory of angular momentum thus greatly simplifies the spherical quantum dot and the cylindrical quantum wire bandstructure calculations. Additionally, for the cylindrical quantum wire, the more accurate axial approximation may be invoked to incorporate band-warping effects.

Utilizing the two-particle model to develop unitary basis transformations, we recast the **K·P** band structure Hamiltonian into a coupled total angular momentum basis for the quantum dot and an uncoupled basis of eigenstates of F_z for the quantum wire. The resulting Hamiltonians are block diagonal, producing eigenstates corresponding to the familiar conduction, light-hole, heavy-hole, and split-off bands. Quantum dot and wire eigenstates are formed by constructing linear superpositions of the bulk crystal eigenstates inside and outside the structures. By matching these functions at the heterointerface, we obtain simple dispersion relations giving the allowed state energies. A two-band dispersion relation was developed and solved for quantum-dot conduction-band states in GaAs/Al$_x$Ga$_{1-x}$As and the type-II system InAs/GaSb. We found good agreement between the two-band model and the less accurate one-band model for GaAs/Al$_x$Ga$_{1-x}$As, but the one-band model failed for the type-II system. For the valence-band states in GaAs/Al$_x$Ga$_{1-x}$As quantum wires and dots, the one-band approximation breaks down completely. The multiple-band calculation, which we introduced, shows that the valence-band states in the quantum dot and quantum wire are admixtures of light- and heavy-hole character. This admixture has a significant affect on the binding energy of valence-band states in quantum dots and on valence subband dispersion in quantum wires, which is highly nonparabolic and electronlike in some cases. Analytic expressions derived in this paper for quantum dot and wire eigenstates rigorously include band-coupling effects and can be used to accurately calculate matrix elements for optical transitions in a straightforward way. The formalism should also greatly simplify the incorporation of band-coupling effects into exciton studies. Further work is in progress to investigate the effect of band-warping terms, neglected in this study, on transport characteristics and optical properties of quantum dots and wires.

TABLE V. The full 8×8 $\mathbf{K} \cdot \mathbf{P}$ Hamiltonian $H(\mathbf{K})$ representing coupling between conduction and valence bands as well as indirect coupling through remote bands. The symbols are defined in the text.

$\|\tfrac{1}{2},\tfrac{1}{2},(0)\rangle$	$\|\tfrac{1}{2},-\tfrac{1}{2},(0)\rangle$	$\|\tfrac{3}{2},\tfrac{3}{2}\rangle$	$\|\tfrac{3}{2},\tfrac{1}{2}\rangle$	$\|\tfrac{3}{2},-\tfrac{1}{2}\rangle$	$\|\tfrac{3}{2},-\tfrac{3}{2}\rangle$	$\|\tfrac{1}{2},\tfrac{1}{2},(1)\rangle$	$\|\tfrac{1}{2},-\tfrac{1}{2},(1)\rangle$
$E_c + \tfrac{1}{2}K^2$	0	$\dfrac{-iPK_+}{\sqrt{2}}$	$i\sqrt{2/3}PK_z$	$i\dfrac{PK_-}{\sqrt{6}}$	0	$-i\sqrt{1/3}PK_z$	$-i\sqrt{1/3}PK_-$
0	$E_c + \tfrac{1}{2}K^2$	0	$-i\dfrac{PK_+}{\sqrt{6}}$	$i\sqrt{2/3}PK_z$	$\dfrac{iPK_-}{\sqrt{2}}$	$-i\sqrt{1/3}PK_+$	$i\sqrt{1/3}PK_z$
$\dfrac{iPK_-}{\sqrt{2}}$	0	$E_v + \dfrac{T}{2}$	$-iL$	$-M$	0	$\dfrac{iL}{\sqrt{2}}$	$\sqrt{2}M$
$-i\sqrt{2/3}PK_z$	$i\dfrac{PK_-}{\sqrt{6}}$	iL^*	$E_v + \dfrac{T}{6} + \dfrac{2Q}{3}$	0	$-M$	$\dfrac{T-2Q}{3\sqrt{2}}$	$-i\sqrt{3/2}L$
$-i\dfrac{PK_+}{\sqrt{6}}$	$-i\sqrt{2/3}PK_z$	$-M^*$	0	$E_v + \dfrac{T}{6} + \dfrac{2Q}{3}$	iL	$i\sqrt{3/2}L^*$	$-\dfrac{T-2Q}{3\sqrt{2}}$
0	$\dfrac{-iPK_+}{\sqrt{2}}$	0	$-M^*$	$-iL^*$	$E_v + \dfrac{T}{2}$	$-\sqrt{2}M^*$	$\dfrac{-iL^*}{\sqrt{2}}$
$i\sqrt{1/3}PK_z$	$i\sqrt{1/3}PK_-$	$\dfrac{-iL^*}{\sqrt{2}}$	$\dfrac{T-2Q}{3\sqrt{2}}$	$-i\sqrt{3/2}L$	$-\sqrt{2}M$	$E_v - \Delta + \dfrac{T+Q}{3}$	0
$i\sqrt{1/3}PK_+$	$-i\sqrt{1/3}PK_z$	$\sqrt{2}M^*$	$i\sqrt{3/2}L^*$	$-\dfrac{T-2Q}{3\sqrt{2}}$	$\dfrac{iL}{\sqrt{2}}$	0	$E_v - \Delta + \dfrac{T+Q}{3}$

APPENDIX: THE CONVENTIONAL K·P HAMILTONIAN

In this section we present the conventional $\mathbf{K} \cdot \mathbf{P}$ band-structure Hamiltonian describing coupling among the two conduction and six valence bands. We use a somewhat different phase convention in our definition of the band-edge Bloch states than that used by other investigators. The states $|J,J_z\rangle$ are written below in terms of orbital wave functions transforming as s states (the conduction bands), p states (the valence bands), and the spin states up and down. Our phase convention is determined by the reality of the Clebsch-Gordan coefficients used to combine the spin and orbital angular momenta to form states of total Bloch angular momentum J:

$$|\tfrac{1}{2},\tfrac{1}{2},(0)\rangle = |s\rangle|\uparrow\rangle \ ,$$

$$|\tfrac{1}{2},-\tfrac{1}{2},(0)\rangle = |s\rangle|\downarrow\rangle \ ,$$

$$|\tfrac{1}{2},\tfrac{1}{2},(1)\rangle = -\sqrt{1/3}[\,|z\rangle|\uparrow\rangle + (|x\rangle + i|y\rangle)|\downarrow\rangle\,] \ ,$$

$$|\tfrac{1}{2},-\tfrac{1}{2},(1)\rangle = \sqrt{1/3}[\,|z\rangle|\downarrow\rangle - (|x\rangle - i|y\rangle)|\uparrow\rangle\,] \ ,$$

$$|\tfrac{3}{2},\tfrac{3}{2}\rangle = -\sqrt{1/2}[\,|x\rangle + i|y\rangle\,]|\uparrow\rangle \ , \tag{A1}$$

$$|\tfrac{3}{2},\tfrac{1}{2}\rangle = \sqrt{2/3}|z\rangle|\uparrow\rangle - \sqrt{1/6}(|x\rangle + i|y\rangle)|\downarrow\rangle \ ,$$

$$|\tfrac{3}{2},-\tfrac{1}{2}\rangle = \sqrt{1/6}(|x\rangle - i|y\rangle)|\uparrow\rangle] + \sqrt{2/3}[\,|z\rangle|\downarrow\rangle \ ,$$

$$|\tfrac{3}{2},\tfrac{3}{2}\rangle = \sqrt{1/2}[\,|x\rangle - i|y\rangle\,]|\downarrow\rangle \ .$$

We include the orbital angular momentum quantum number in parentheses for the conduction and split-off bands to distinguish between the two. For these bands the following correspondences apply between the band-edge representations of the crystal double group and the representations of the full rotation group (written D_j, corresponding to the states that transform an angular momentum j): $D_{1/2} \leftrightarrow \Gamma_6$ for conduction band, $D_{1/2} \leftrightarrow \Gamma_7$ for the split-off bands, and $D_{3/2} \leftrightarrow \Gamma_8$ corresponding to

the coupled light and heavy holes.

In this basis, the Hamiltonian matrix $\underline{H}(\mathbf{K})$ takes the form given in Table V. E_c, E_v, Δ have their usual meanings, P is the Kane momentum matrix element, and the other terms are defined as follows:

$$K^2 = K_x^2 + K_y^2 + K_z^2 \ ,$$

$$K_+ = K_x + iK_y \ ,$$

$$K_- = K_x - iK_y \ ,$$

$$\frac{-T}{2} = (\gamma_1 + \gamma_2)\frac{(K_x^2 + K_y^2)}{2} + (\gamma_1 - 2\gamma_2)\frac{K_z^2}{2} \ , \tag{A2}$$

$$-\left[\frac{T}{6} + \frac{2Q}{3}\right] = (\gamma_1 - \gamma_2)\frac{(K_x^2 + K_y^2)}{2} + (\gamma_1 + 2\gamma_2)\frac{K_z^2}{2} \ ,$$

$$-L = \begin{cases} -i2\sqrt{3}\gamma_3\dfrac{(K_x - iK_y)K_z}{2} \\ \text{(axial approximation)}, \\ -i2\sqrt{3}\gamma_2\dfrac{(K_x - iK_y)K_z}{2} \\ \text{(spherical approximation)}, \end{cases}$$

$$-M = \sqrt{3}\gamma_2\frac{(K_x - iK_y)^2}{2} \ .$$

The γ parameters in these expressions are so-called modified Luttinger parameters which are related to the true Luttinger coupling parameters[27] by the relations[29]

$$\gamma_1 = \gamma_1^{\text{true}} - \frac{2P^2}{3(E_c - E_v)} \ ,$$

$$\gamma_2 = \gamma_2^{\text{true}} - \frac{P^2}{3(E_c - E_v)} \ , \tag{A3}$$

$$\gamma_3 = \gamma_3^{\text{true}} - \frac{P^2}{3(E_c - E_v)} \ .$$

In these modified parameters we have effectively subtracted out the effects of valence-band coupling to the conduction bands from the true parameters. These effects are included explicitly in this model. Note that we have also assumed inversion symmetry in this Hamiltonian.

We note that a number of simplifications are possible. We can restrict attention solely to the Γ_8 block, for example, in which case we simply obtain Luttinger's 4×4 Hamiltonian[27] and the true Luttinger parameters are used in place of the modified parameters discussed above. In the spherical approximation, this gives isotropic LH

and HH dispersions

$$E_{HH}(K)=E_v-(\gamma_1-2\gamma_2)\frac{K^2}{2} , \tag{A4}$$

$$E_{LH}(K)=E_v-(\gamma_1+2\gamma_2)\frac{K^2}{2} . \tag{A5}$$

where $K=|\mathbf{K}|$. On the other hand, if we neglect the Luttinger coupling parameters and the free-electron kinetic-energy term $K^2/2$ entirely, we recover the Kane dispersion relations discussed in the text.[24]

[1]Peter C. Sercel and Kerry J. Vahala, in *The International Electronics Conference, 1990, Technical Digest Series* (Optical Society of America, Washington, D.C., 1990), Vol. 8, pp. 204–205.

[2]Kerry J. Vahala and Peter C. Sercel, Phys. Rev. Lett. **65**, 239 (1990).

[3]D. Schecter, J. Phys. Chem. Solids **23**, 237 (1962).

[4]A. Baldereschi and Nunzio O. Lipari, Phys. Rev. B **8**, 2697 (1973).

[5]A. Baldereschi and Nunzio O. Lipari, Phys. Rev. B **9**, 1525 (1974).

[6]Masahiro Asada, Yasuyuki Miyamoto, and Yasuharu Suematsu, Jpn. J. Appl. Phys. **24**, L95 (1985).

[7]Yasuhiko Arakawa, Kerry Vahala, and Amnon Yariv, Appl. Phys. Lett. **45**, 950 (1984).

[8]Takeshi Kodama, Yukio Osaka, and Masamichi Yamanishi, Jpn. J. Appl. Phys. **24**, 1370 (1985).

[9]Marcos H. Degani and Oscar Hipolito, Phys. Rev. B **35**, 9345 (1987).

[10]Jerry W. Brown and Harold N. Specter, Phys. Rev. B **35**, 3009 (1987).

[11]A. Fasolino and M. Altarelli, in *Two-Dimensional Systems, Heterostructures, and Superlattices* (Springer-Verlag, New York, 1984).

[12]J. A. Brum, G. Bastard, L. L. Chang, and L. Esaki, Superlatt. Microstruct. **3**, 47 (1987).

[13]Ikuo Suemune and Larry A. Coldren, IEEE J. Quantum Electron. **QE-24**, 1778 (1988).

[14]D. S. Citrin and Yia-Chung Chang, Phys. Rev. B **40**, 5507 (1989).

[15]Kerry J. Vahala, IEEE J. Quantum Electron. **QE-24**, 523 (1988).

[16]Hal Zarem, Kerry J. Vahala, and Amnon Yariv, IEEE J. Quantum Electron. **QE-25**, 705 (1989).

[17]G. T. Einevoll and Y.-C. Chang, Phys. Rev. B **40**, 9683 (1989).

[18]G. R. Olbright, N. Peyghambarian, S. W. Koch, and L. Banyai, Opt. Lett. **12**, 413 (1987).

[19]Louis Brus, IEEE J. Quantum Electron. **QE-22**, 1909 (1986).

[20]E. Kapon, D. M. Hwang, and R. Bhat, Phys. Rev. Lett. **63**, 430 (1989).

[21]John A. Lebens, Charles Tsai, Kerry J. Vahala, and Thomas Kuech, Appl. Phys. Lett. **56**, 2642 (1990).

[22]Mark Sweeny, Jingming Xu, and Michael Shur, Superlatt. Microstruct. **4**, 623 (1988).

[23]M. Sweeny and Jingming Xu, Solid State Commun. **72**, 301 (1989).

[24]Evan O. Kane, J. Phys. Chem. Solids **1**, 249 (1957).

[25]E. O. Kane, in *Physics of III-V Compounds*, Vol. 1 of *Semiconductors and Semimetals*, edited by R. K. Willardson and Albert C. Beer (Academic, New York, 1966), p. 75.

[26]J. M. Luttinger and W. Kohn, Phys. Rev. **97**, 869 (1955).

[27]J. M. Luttinger, Phys. Rev. **102**, 1030 (1956).

[28]Amnon Yariv, *Quantum Electronics*, 3rd ed. (Wiley, New York, 1989), Chaps. 11 and 12.

[29]C. R. Pidgeon and R. N. Brown, Phys. Rev. **146**, 575 (1966).

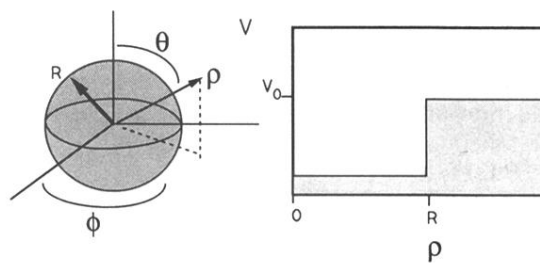[30]S. R. White and L. J. Sham, Phys. Rev. Lett. **47**, 879 (1981).

[31]G. A. Sai-Halasz, R. Tsu, and L. Esaki, Appl. Phys. Lett. **30**, 651 (1977).

[32]L. L. Chang, N. Kawai, G. A. Sai-Halasz, R. Ludeke, and L. Esaki, Appl. Phys. Lett. **35**, 939 (1979).

[33]M. Altarelli, Phys. Rev. B **28**, 842 (1983).

[34]Peter C. Sercel and Kerry J. Vahala (unpublished).
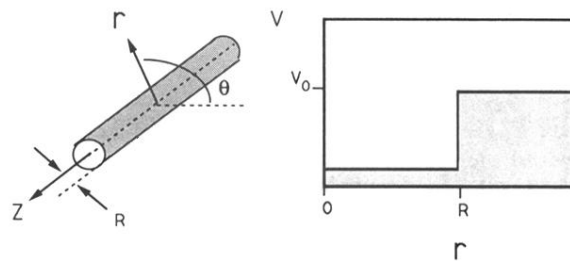
Spherical Quantum Dot:

Cylindrical Quantum Wire:

FIG. 2. A cylindrical quantum wire and a spherical quantum dot. The drawings to the left represent the structures, those to the right represent the confining potential as a function of the radial coordinate in each case. The well depth, V_0 in the figure, represents a discontinuity of the band edges across the hetero-structure interface.